

AD-A163 604

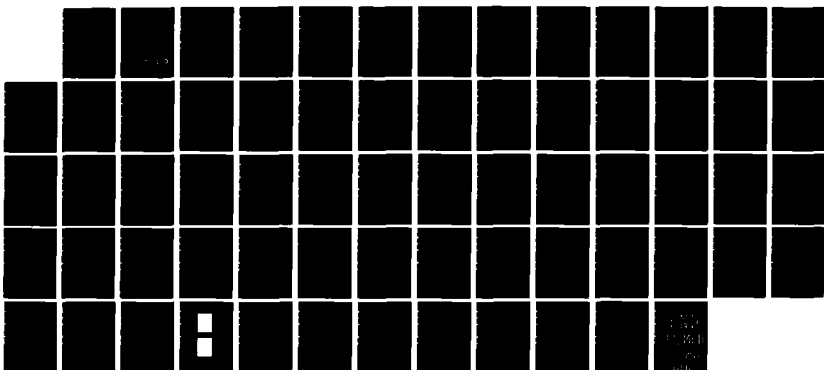
LASER INTERACTION IN LONG-SCALELENGTH PLASMAS(U) NAVAL  
RESEARCH LAB WASHINGTON DC J H GARDNER ET AL  
31 DEC 85 NRL-MR-5651

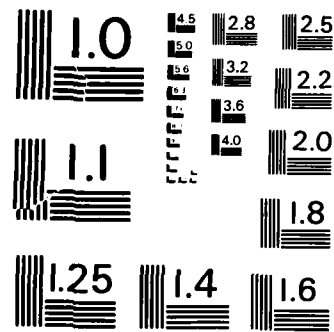
1/1

UNCLASSIFIED

F/G 20/9

NL





MICROCOPY RESOLUTION TEST CHART  
NATIONAL BUREAU OF STANDARDS - 1963 - A

2

NRL Memorandum Report 5651

## Laser Interaction in Long-Scalelength Plasmas

J. H. GARDNER, M. J. HERBST,\* F. C. YOUNG,\*\* J. A. STAMPER,\* S. P. OBENSCHAIN,\*  
C. K. MANKA,\* K. J. KEARNEY,\* J. GRUN,\* D. DUSTON,† AND P. G. BURKHALTER§

*Laboratory for Computational Physics*

*\*Laser Plasma Branch  
Plasma Physics Division*

*\*\*Plasma Technology Branch  
Plasma Physics Division*

*†Plasma Radiation Branch  
Plasma Physics Division*

*§Condensed Matter Physics Branch  
Condensed Matter and Radiation Sciences Division*

AD-A163 604

December 31, 1985



DTIC  
ELECTED  
FEB 05 1986  
S E D

FILE COPY  
FILE COPY

NAVAL RESEARCH LABORATORY  
Washington, D.C.

Approved for public release; distribution unlimited.

86 25 018

AD-A163604

SECURITY CLASSIFICATION OF THIS PAGE

## REPORT DOCUMENTATION PAGE

1a. REPORT SECURITY CLASSIFICATION UNCLASSIFIED		1b. RESTRICTIVE MARKINGS	
2a. SECURITY CLASSIFICATION AUTHORITY		3. DISTRIBUTION/AVAILABILITY OF REPORT	
3b. DECLASSIFICATION / DOWNGRADING SCHEDULE		Approved for public release; distribution unlimited.	
4. PERFORMING ORGANIZATION REPORT NUMBER(S) NRL Memorandum Report 5651		5. MONITORING ORGANIZATION REPORT NUMBER(S)	
6a. NAME OF PERFORMING ORGANIZATION Naval Research Laboratory	6b. OFFICE SYMBOL (If applicable) Code 4040	7a. NAME OF MONITORING ORGANIZATION Department of Energy	
6c. ADDRESS (City, State, and ZIP Code) Washington, DC 20375-5000		7b. ADDRESS (City, State, and ZIP Code) Washington, DC 20545	
8a. NAME OF FUNDING / SPONSORING ORGANIZATION Department of Energy	8b. OFFICE SYMBOL (If applicable)	9. PROCUREMENT INSTRUMENT IDENTIFICATION NUMBER	
8c. ADDRESS (City, State, and ZIP Code) Washington, DC 20545		10. SOURCE OF FUNDING NUMBERS	
PROGRAM ELEMENT NO.	PROJECT NO.	TASK NO.	WORK UNIT ACCESSION NO.
		81425	44-0859-A-5
11. TITLE (Include Security Classification) Laser Interaction in Long-Scalelength Plasmas			
12. PERSONAL AUTHOR(S) Gardner, J.H., Herbst, M.J., Young, F.C., Stamper, J.A., Obenschain, S.P., Manka, C.K., Kearney, K.J., Grun, J., Duston, D., and Burkhalter, P.G.			
13a. TYPE OF REPORT Interim	13b. TIME COVERED FROM _____ TO _____	14. DATE OF REPORT (Year, Month, Day) 1985 December 31	15. PAGE COUNT 66
16. SUPPLEMENTARY NOTATION			
17. COSATI CODES		18. SUBJECT TERMS (Continue on reverse if necessary and identify by block number)	
FIELD	GROUP	SUB-GROUP	Long Scalelength Stimulated Brillouin Backscatter, Laser Plasma Interaction Laser absorption ←
19. ABSTRACT (Continue on reverse if necessary and identify by block number)			
Absorption of a short-pulse, high-intensity Nd-laser beam (vacuum irradiance of $10^{14}$ to $10^{15}$ W/cm <sup>2</sup> ) by preformed plasmas of different density scalelengths is investigated. Increased effects of plasma instabilities are found at longer scalelengths. The amount of backscattered light increases with plasma scalelength and limits the absorption fraction at the longest scalelength. The onset of suprathermal electron production, deduced from observations of energetic (20 to 50 keV) x rays, occurs at lower laser irradiance for longer scalelength plasmas. A correlation between energetic x rays and $3\omega_0/2$ emission suggests that the suprathermal electrons are produced by a plasma instability at quarter-critical density. At higher intensities there is evidence for severe perturbations of the preformed plasma and for self-focusing of the incident beam. (10)			
20. DISTRIBUTION/AVAILABILITY OF ABSTRACT <input checked="" type="checkbox"/> UNCLASSIFIED/UNLIMITED <input type="checkbox"/> SAME AS RPT. <input type="checkbox"/> DTIC USERS		21. ABSTRACT SECURITY CLASSIFICATION UNCLASSIFIED	
22a. NAME OF RESPONSIBLE INDIVIDUAL John H. Gardner		22b. TELEPHONE (Include Area Code) (202) 767-6582	22c. OFFICE SYMBOL Code 4040

DD FORM 1473, 84 MAR

33 APR edition may be used until exhausted.  
All other editions are obsolete.

SECURITY CLASSIFICATION OF THIS PAGE

## CONTENTS

I. INTRODUCTION .....	1
II. EXPERIMENTAL SETUP .....	4
III. SCATTERED LIGHT AND ABSORPTION EFFICIENCY .....	7
IV. GENERATION OF ENERGETIC ELECTRONS .....	14
V. PERTURBATIONS TO THE PLASMA AND SELF-FOCUSING .....	23
VI. SUMMARY AND CONCLUSIONS .....	30
VII. ACKNOWLEDGMENTS .....	34
APPENDIX I — Brillouin Backscatter Calculation .....	35
REFERENCES .....	59

Accession For	
NTIS GRA&I	<input checked="" type="checkbox"/>
DTIC TAB	<input type="checkbox"/>
Unannounced	<input type="checkbox"/>
Justification	
By _____	
Distribution/ _____	
Availability Codes	
Dist	Avail and/or Special
A-1	



## LASER INTERACTION IN LONG-SCALELENGTH PLASMAS

### I. INTRODUCTION

Of the five critical elements for high-gain laser-driven fusion,<sup>1</sup> coupling efficiency and cold-fuel isentrope are directly related to laser absorption in the underdense plasma surrounding the fuel pellet. Absorption efficiency is important because it is directly related to the overall gain of the system. Cold-fuel isentrope is related to absorption because some absorption mechanisms preferentially produce energetic particles ( $\gg 10$  keV) which may penetrate the outer pellet, preheat the fuel, and prevent the high fuel compressions required for high-gain systems.

Classical collisional absorption is the preferred absorption mechanism for laser fusion because it results in a low-temperature ( $\leq 5$  keV) thermal particle distribution of the absorbed energy. Moreover, collisional or inverse bremsstrahlung absorption is predicted by theory<sup>2</sup> and computer simulations<sup>3</sup> to provide high absorption efficiency in the large underdense plasmas expected with high-gain pellets. Unfortunately, parametric instabilities may also occur in these larger plasmas.<sup>4</sup> For example, the stimulated Brillouin scattering (SBS) instability<sup>5</sup> can reduce the absorption efficiency by reflecting the incident light before it is absorbed. Stimulated Raman scattering<sup>6-8</sup> and the two-plasmon decay ( $2\omega_p$ ) instability<sup>9</sup> can couple laser energy more efficiently into the plasma, but this absorbed energy is preferentially deposited into energetic particles. Finally, thermal<sup>10</sup> and ponderomotive<sup>10,11</sup> self-focusing are enhanced in longer

scalelength plasmas and self-focusing can increase the role of these parametric instabilities.

The relative importance of collisional absorption and the various parametric instabilities depends upon the plasma density ( $n$ ) and temperature ( $T$ ) and the plasma scalelengths for density, temperature, and velocity ( $L_n = |n/\nabla n|$ ,  $L_T = |T/\nabla T|$ ,  $L_u = |u/\nabla u|$ ). Presently available laser systems lack the energy required to produce both the long scalelength and high density and temperature that will be typical of plasmas surrounding large high-pellets; therefore, the relative importance of the various absorption processes in present experiments is likely to be different from that in high-gain systems. To predict whether the deleterious effects of increased plasma instabilities in these larger plasmas negate the beneficial effects of increased collisional absorption, it is important to understand the changing roles of these processes as plasma scalelengths are increased.

For a given laser energy, many clever schemes have been developed to produce longer scalelength plasmas than those that are available from solid target ablation;<sup>12-27</sup> however, controlled variations of plasma scalelength have not been incorporated in experiments using these schemes. Indirect evidence for increased collisional absorption and plasma instabilities at longer scalelength has been obtained in solid target experiments by 1) varying the laser pulse duration,<sup>28-30</sup> 2) varying the focal spot size for a given laser-target configuration,<sup>31-34</sup> and 3) allowing prepulses to irradiate the target before the arrival of the main laser pulse.<sup>35-37</sup> As laser systems have become more energetic, larger underdense plasmas have been produced with  $L_n/\lambda_0$  ( $\lambda_0$  is the laser wavelength) up to 500 at one-tenth critical density ( $n_c/10$ ).<sup>38-40</sup> In these longer-scalelength plasmas,

increased effects of plasma instabilities have been inferred by comparing results with those of shorter-scalelength plasmas produced by earlier less energetic laser systems.<sup>41,42</sup>

In the present work, the first experimental study of laser absorption with controlled variations of plasma scalelength is reported. A novel configuration of two laser beams is used which allows the production of a long-scalelength plasma by one beam and the subsequent irradiation of that plasma by a second, high-intensity pulse. Underdense plasmas with  $L_n/\lambda_0$  up to 400 at  $n_c/10$  can be produced. These scalelengths are comparable to those produced by single-beam irradiations with much larger lasers.<sup>42</sup> Moreover, the scalelength of the plasma may be varied independently of the focal condition of the high-intensity beam. This is advantageous because parametric instabilities which are preferentially excited in localized regions of higher intensity or "hot spots" within the focal distribution remain unchanged with the scalelength variations in the present experiment. In experiments where the plasma scalelength is varied by changing the focal condition of the intense beam or by comparing results from different lasers,<sup>43</sup> ambiguities can arise because these hot spots can vary greatly between different focal conditions of a given laser system or between different laser systems.

The experimental arrangement used to produce long-scalelength plasmas is described in Sec. II. In the remainder of the paper we discuss the interaction of high-intensity laser beams with long-scalelength plasmas and derive results which may impact high-gain pellet designs. Scattered light measurements are discussed in Sec. III, and an increase in backscattered light is found to limit absorption efficiency at longer scalelength.<sup>44</sup> Surprisingly, the increase in backscatter with scalelength is not as rapid as might have been expected from linear theory with a constant noise source;

this can be explained by observed reductions in specular scatter, which may be the noise source for SBS growth, at longer scalelength. Measurements of energetic x-rays, indicative of suprathermal-electron production, are presented in Sec. IV. An increase in suprathermal electrons at the longer scalelengths<sup>45</sup> is attributed to parametric instability at quarter-critical density ( $n_c/4$ ). Finally, perturbation of the preformed long-scalelength plasma by the high intensity laser beam and the consequent self-focusing<sup>46</sup> are described in Sec. V. The implications of all of these results are summarized in Sec. VI.

In the parameter regime investigated here, the deleterious effects of plasma instabilities seem to outweigh the beneficial increase in collisional absorption that is observed. While a direct extrapolation of the results of this experiment to high-gain systems must be done with some care, the observed effect of plasma instabilities should be useful to benchmark computational and theoretical models that are used to extrapolate to larger systems.

### III. EXPERIMENTAL SETUP

#### A. Simultaneous Production of Long-Scalelength Plasma and High Laser Intensity

To produce long-scalelength plasmas with controlled and variable scalelengths, planar targets of polystyrene  $[(CH)_x]$  are irradiated at a  $\delta'$  angle of incidence by one beam of a two-beam, neodymium (Nd) glass laser ( $\lambda_0 = 1.054 \mu m$ ) system. This beam has a long pulse-duration (4-nsec FWHM) and irradiates a large focal area at the target (90% of the energy lies within a

diameter  $d_{90} = 1080 \mu\text{m}$ ), giving a peak irradiance of about  $6 \times 10^{12} \text{ W/cm}^2$ . To vary the scalelength of the plasma in a controlled way, this beam is apertured in the near-field to reduce  $d_{90}$  at the target. The increased lateral hydrodynamic expansion from the reduced focal spot on target leads to a reduction in the underdense plasma scalelength, as shown in Sec. II B. Three apertures are used in the present study, corresponding to focal diameters of 360, 640, and  $1080 \mu\text{m}$ . These will be referred to as short, medium, and long-scalelength background plasmas, respectively. By using a nearly constant peak intensity of this beam, the temperature of the preformed plasma (as confirmed by computer simulation and time-integrated and time resolved continuum x-ray spectra) remains nearly the same as the scalelength is varied.

To study the laser-plasma interaction at high irradiance, the second beam of the laser system is tightly focused (50% of the energy is within  $d_{50} = 90 \mu\text{m}$ ) and aligned along the central axis of the first beam, as shown in Fig. 1. Vacuum intensities (averaged over  $d_{50}$ ) from  $10^{14}$  to  $10^{15} \text{ W/cm}^2$  are produced for incident energies between 4 and 40 jcules. Incident energies are quoted in the text because the actual intensities in the plasma may be altered by self-focusing as discussed in Sec. V B. The second beam is synchronous with the peak of the first beam and has a reduced pulse duration (0.3-nsec FWHM) to minimize the hydrodynamic perturbations of the background plasma. Initially, the two laser beams have orthogonal linear polarizations, but passage through a quarter-wave plate produces opposite circular polarizations at the target and converts circularly polarized backscatter into linear polarization before detection.

### 3. Characterization of the Background Plasma

Two-dimensional hydrodynamic calculations are used to predict density, temperature, and velocity profiles of the background plasma, as shown in Figs. 2-4. The computer code used for these calculations is an Eulerian, one-temperature fluid model that solves the equations of fluid motion in cylindrical coordinates. It includes both classical thermal conduction and collisional absorption by inverse bremsstrahlung.<sup>3</sup> The absorption is performed along straight ray paths normal to the target using the cylindrically averaged, radial intensity pattern that is determined experimentally on every laser shot in an equivalent focal plane.<sup>47</sup>

Interferometric measurements provide an experimental check of the background-plasma density profiles up to quarter-critical density ( $n_c/4$ ). These measurements are made along an axis orthogonal to the target normal using a short pulse (0.3-nsec FWHM) of the third harmonic ( $\lambda = 3513 \text{ \AA}$ ) of the incident laser. Abel inversion of the interferograms yields on-axis density profiles up to  $n_c/4$  as shown in Figs. 2A-C. In Figs. 2A and 2B, the apparent shift of the interferometric data to smaller distances  $z$  than the calculated profiles is not significant; a slight curvature of the target or small errors in target tilt relative to the interferometric axis (given the size target foils used) could cause errors in locating the absolute position of the target ( $z=0$ ). The shapes of the measured density profiles, however, confirm the code-predicted density scalelengths for the three background plasmas at densities  $n < n_c/4$ .

Confirmation of the calculated temperature profile and the density profile up to  $n = 2n_c$  in the long-scalelength background plasma is obtained from x-ray spectroscopic measurements. The data shown in Figs. 2C and 3C are obtained by spot spectroscopy<sup>47-49</sup> with aluminum tracer dots. Only the

longest scalelength plasma can be diagnosed in this manner; the more rapid change of plasma parameters seen by ions flowing through the medium in short scalelength plasmas invalidates the interpretation of the spectroscopic line ratios used to measure the density and temperature for these plasmas<sup>50</sup>. Spectroscopic densities are within a factor of two of those from the code and interferometry. At least some of this discrepancy may be explained by the averaging of the spectroscopic diagnostic over the laser pulse, in contrast to the instantaneous values at the peak of the pulse from the code and interferometry. The underdense-plasma scalelengths from all three of these techniques are in essential agreement.

### III. SCATTERED LIGHT AND ABSORPTION EFFICIENCY

Experimentally, the absorption of the high-intensity beam is inferred from measurements of scattered light. Light scattered outside the incident lens cone is attributed to specular reflection of non-absorbed light at the critical-density surface, as discussed in Sec. III A. Stimulated Brillouin scattering (SBS) is believed to be responsible for light directly backscattered through the lens, as outlined in Sec. III B. In Sec. III C, comparisons are made between experimental absorption fractions and the predictions of the hydrodynamic computer model. The variation of absorption with plasma scalelength is discussed in Sec. III D.

#### A. Scattered Light Outside the Lens Cone

Scattered light at angles outside the incident focal cone is measured with an array of five diodes with subnanosecond response time: four detectors are deployed on one side of the specular angle( $12^\circ$ ) in the plane

of incidence of the laser, and a fifth detector samples light on the other side. If we assume symmetry about the specular direction, angular distributions of the scattered light are determined, as shown in Fig. 5. With this assumption, integrations over angle yield the total reflectivity of light outside the incident focal cone, as shown in Figs. 5B-D. The intensity of this light increases with increasing laser energy and decreases with increasing background plasma scalelength.

The data in Fig. 5 are consistent with the hypothesis that this non-absorbed light has been specularly reflected from the critical-density surface. The decreased reflectivity at the longer scalelength can be explained by increased collisional absorption, which reduces the penetration of incident light to critical density and reflected light to the detectors. The increase in reflectivity at higher incident energies can be explained by increased plasma heating, which reduces collisional absorption. This hypothesis is supported by predictions of collisional absorption by hydrocode calculations (as discussed in Sec. III C); observed levels of light scattered outside the lens are close to code predictions for specular scatter of non-absorbed light.

### B. Backscattered Light

Laser light backscattered through the incident f/6.7 lens is observed with both time-resolving and time-integrating detectors. A photodiode with a risetime of 0.7 nsec distinguishes the short-pulse backscatter from the lower-level, longer-duration backscatter of the background beam. The reflectivities quoted in this paper are based upon integrated energies of the short pulse backscatter because the detector cannot time-resolve the short pulse. Two calorimeters are used in conjunction with a polarizing

beamsplitter to determine the total backscattered energy in each of two polarizations. The short-pulse backscatter is found to be preferentially polarized with the same polarization as that of the high-intensity beam, unlike the unpolarized backscatter of the background beam. Backscatter reflectivities, shown in Fig. 6, increase with increasing incident short pulse energy up to 15 Joules, but decrease with further increase of the incident energy.

Three observed properties of the backscatter are consistent with production by Stimulated Brillouin Scattering(SBS): 1) the backscattered light has the polarization of the incident beam, 2) the reflectivities (at least at low incident energies) increase with incident energy, and 3) the rate of this increase becomes larger with longer background-plasma scalelength. However, two other characteristics of the backscatter seem inconsistent with SBS: 1) at higher incident energies, the reflectivity decreases with increasing energy, and 2) the backscatter reflectivity in the long-scalelength plasma is only about twice that in the short-scalelength plasma, although the number of linear SBS e-foldings should be nearly proportional to the plasma scalelength.

The decrease in backscatter reflectivity at the higher incident energies may be consistent with SBS if strong plasma perturbations at the higher incident energies are taken into account. An axial shock produced by the increased mass ablation rate is predicted by the hydrodynamic code at the higher incident energies (see Sec. V A). Abrupt changes in the plasma flow velocity and reduced plasma scalelengths that result from this shock could reduce the Brillouin growth length and thereby the Brillouin backscatter. Furthermore, the possible effect on SBS of self-focusing at the higher incident energies (see Sec. V B and Ref. 46) is difficult to

assess. An increased angular spread of the backscatter may occur, causing a reduction in the reflectivity observed through the incident lens. The overflow of backscattered light into angles just outside the incident lens cone cannot be ruled out because scattered light is not monitored there (the location of the diode nearest the lens cone can be seen from Fig. 5A to be about  $7^{\circ}$  from the edge of the lens cone).

The second apparent inconsistency with SBS, the fact that the backscatter reflectivity merely doubles as the plasma scalelength doubles, can also be explained. A simple model for calculating Brillouin backscatter, described in detail in Appendix I, predicts that the theoretical number of e-foldings in the long-scalelength plasma is 3.6 greater than that calculated for the short-scalelength plasma. However, this large difference in Brillouin growth may be partially offset by a difference in the noise level from which the instability grows. Specularly scattered light, a likely noise source for SBS growth, is reduced in the long-scalelength plasma by about one order of magnitude relative to the level in the short-scalelength case. As explained in Appendix I, the number of e-foldings required to amplify the experimentally observed specular reflection up to the level of the observed backscatter is within the 10% uncertainty of the number of SBS e-folds that is theoretically predicted for both the long and short-scalelength plasmas. For the short-scalelength plasmas, 6.4 linear e-folds would be required to amplify the specular level of  $1.25 \times 10^{-4}$  (this is the portion of the measured specular scatter that reflects into the incident focal cone) up to the observed 5.5% backscatter level at 5J or  $10^{14} \text{ W/cm}^2$  (in vacuum); this is very close to the 6.6 e-folds of SBS growth that is calculated for conditions of the short-scalelength plasma. Similarly, it is found that 9.4 e-folds would be needed to account for the 8% backscatter reflectivity at  $10^{14} \text{ W/cm}^2$  in the long-scalelength

plasma, given the reduced specular level in that case. This compares well with the 10.2 e-folds calculated in Appendix I for the long-scalelength plasma. Thus, the observed increase in backscatter with plasma scalelength is entirely consistent with SBS theory if the noise source for SBS growth is specularly reflected light.

Of course, this interpretation assumes that the high-intensity beam does not self-focus at these low incident energies. Experimentally, self-focusing is inferred from  $2\omega_0$  images only for  $E > 14$  J (see Sec. VB and ref. 46); however, steady-state beam propagation calculations that agree with these experimental observations also suggest self-focusing at lower energies.<sup>46</sup> It is not possible, therefore, to absolutely rule out self-focusing as a factor in this study. Self-focusing complicates the backscatter interpretation because: 1) near a focus, self-focusing both increases the SBS gain coefficient due to the increase in intensity and reduces it due to the decrease in density and increase in temperature, 2) the SBS gain coefficient may also be reduced in regions where the beam intensity is reduced due to divergence from a focus, which might have been the optimal SBS growth regions before self-focusing, and 3) the total number of SBS e-foldings, due to the integration of the gain coefficient over the interaction region, may be reduced if the depth-of-focus of the self-focusing limits the interaction region more severely than the inhomogeneity-induced phase mismatch. Whether the net effect of self-focusing is to increase or decrease SBS depends upon the complicated interplay between these effects.

### C. Absorption Efficiency

The experimentally defined absorption fraction for the short pulse is given as  $\eta = 1-R-S$ , where where  $R$  is the reflectivity of backscatter through the lens (see Sec. III B) and  $S$  is the integrated reflectivity over other angles (see Sec. III A). Values of  $\eta$  inferred from the data of Figs. 5 and 6 are displayed in Fig 7. Unfortunately, the configuration of the experiment precludes a direct check of these absorption fractions by plasma calorimetry. The quantity of interest, the absorbed energy due to the short-pulse, high-intensity beam, is buried within the larger amount of energy associated with the long-pulse beam.

These experimental absorption fractions are compared with values from the hydrodynamic simulations. Because the code does not treat plasma instabilities, the incident energy used in the simulations is reduced by the observed backscatter in order to model reflections that occur in the underdense plasma. Thus, an energy  $E' = E(1-R)$  is used to model an experiment with an incident laser energy  $E$ . The simulation indicates that a fraction  $f'$  of the energy  $E'$  is collisionally absorbed and the remainder is specularly reflected. For comparison with the experimental absorption fraction  $\eta$ , it is necessary to calculate the ratio of the absorbed energy  $f'E'$  to the incident energy  $E$ ; this gives the code-predicted absorption fraction  $f = f'(1-R)$ . These calculated absorption fractions are compared to the experimental values in Fig. 7. The calculated absorption fractions are consistent with or slightly smaller than the experimental values, but by no more than 10% of the incident energy. The near agreement between the calculated absorption fractions  $f$  and the experimental absorption fractions  $\eta$  indicates that the absorption of non-backscattered light can be attributed almost entirely to collisional absorption. There are at least three

possible explanations for experimental absorption fractions that slightly exceed the calculated fractions: 1) with the limited number of detectors, some of the scattered light might not be detected, causing an overestimate of the experimental absorption fractions, 2) the calculations might underestimate the collisional absorption since the code results have slightly higher temperatures than are measured (see Sec. V A), and 3) absorption mechanisms other than collisional absorption may be operative. None of these alternatives significantly affects the inferred absorption fractions, although item (3) raises concern about the generation of suprathermal electrons by the additional absorption mechanism(s), as discussed in Sect. IV.

#### D. Variation of Absorption with Plasma Scalelength

The overall absorption efficiency in the experiment does not vary significantly with plasma scalelength, as indicated in Figs 7A-C. As discussed in Sec. III C, the absorption fractions can be almost entirely explained by a combination of classical absorption and a backscatter instability in the underdense plasma. The important variation of absorption with plasma scalelength becomes evident upon examination of the relative role of these two processes in determining the overall absorption efficiency.

For example, at  $E = 12 \text{ J}$  (corresponding to a vacuum irradiance of  $3 \times 10^{14} \text{ W/cm}^2$ ), Figs. 8A and 8B show that the backscatter reflectivity  $R$  and specular reflectivity  $S$  are 10.8% and 9%, respectively, for the short-scalelength plasma. Therefore, these two effects are contributing nearly equally in limiting the overall absorption  $n = 1 - R - S$  to 80%. Even if there were no backscatter, the imperfect efficiency of collisional

absorption would prevent total absorption of the incident laser light. A different picture emerges at long scalelength, where the backscatter reflectivity  $R = 18\%$  and specular reflectivity  $S = 2.5\%$  at  $E = 12 \text{ J}$ . Without backscatter, the increased efficiency of collisional absorption  $1 - S$  would cause nearly total absorption of the incident laser beam. Therefore, the backscatter reflectivity  $R$  has become the dominant factor in limiting the total absorption  $\eta = 1 - R - S$  to 80% in the long-scalelength case.

A naive extrapolation of the trend of Figs. 8A and 8B to even longer scalelengths would imply that the increased backscatter would begin to drastically reduce the overall absorption efficiency despite an increasing effectiveness of collisional absorption (unless collisional absorption became so efficient at low densities that it reduced the incident intensity in the SBS growth region). However, the importance of the noise source for SBS from Sec. III B must be remembered. Because noise sources can decrease at longer plasma scalelengths, simple extrapolation of the present results is not possible; in fact, as the levels of specular reflection decrease due to increased collisional absorption, entirely different noise sources such as enhanced acoustic turbulence may become dominant.

#### IV. GENERATION OF ENERGETIC ELECTRONS

Even though collisional absorption can account for most of the observed absorption, other mechanisms, as mentioned earlier, may preferentially deposit energy in energetic electrons. Even a small fraction of energetic electrons, while not important from the standpoint of absorption efficiency, may cause unacceptable levels in fuel preheat. The exact level of acceptable preheat depends upon the details of specific ICF pellet designs;

however, as little as 0.1% of the incident laser energy deposited into a Maxwellian distribution of suprathermal electrons of sufficient temperature may lead to unacceptable preheat.<sup>1</sup>

#### A. X-RAY SPECTRA

To determine the level of energetic-electron production in this experiment, temporally and spatially integrated spectra of the continuum x-ray emission are measured. Arrays of detectors with K-edge filters<sup>51</sup> are used: seven PIN diodes for the 1-10 keV spectral region and seven scintillator-photomultipliers for the 20-115 keV region. Measurements are made at  $120^0$  to the incident laser-beam direction, and isotropic emission into  $4\pi$  sr is assumed. The three detectors recording x rays greater than 50 keV measure only background levels. X-ray spectra are unfolded from measurements below 50 keV, and electron temperatures are extracted from the slopes of the spectra. Two such spectra are shown in Fig. 9, corresponding to a fixed short-scalelength background plasma but different short-pulse laser energies. Because the detectors are time-integrating, the low energy x-ray emission is biased by the 4-nsec pulse which generates the background plasma and contains a large fraction of the incident laser energy. Consequently, the spectra in Fig. 9 are quite similar at low x-ray energy although at the high short-pulse energy there is consistently higher x-ray emission as should be expected since the short-pulse energy is approaching that of the background beam energy. Average values of the thermal electron temperature, determined from slopes of the 1 to 3 keV spectral region at low short-pulse energy are 285, 300, and 325 eV for the short, medium, and long scalelength plasmas, respectively. These temperatures are nearly equal, as

predicted by hydrodynamic calculations, because the irradiance of the 4-nsec pulse is held nearly constant as the scalelength is changed.

Energetic electron production is inferred from a high-energy tail on the continuum x-ray spectrum. This emission is sensitive to the short-pulse laser energy, as shown in Fig. 9. In the low-energy case (7.6 J, corresponding to  $1.9 \times 10^{14} \text{ w/cm}^2$  in vacuum), this emission is less than experimental detection limits, as shown by the dashed line in Fig. 9. The 4-nsec laser pulse gives no detectable high-energy emission because it is at too low an irradiance. At higher short-pulse energy (e.g., 21 J, corresponding to  $5.3 \times 10^{14} \text{ w/cm}^2$  in vacuum), x-rays with energies greater than 20 keV are observed, indicative of the presence of suprathermal electrons. This emission increases with laser energy as well as with background-plasma scalelength, as discussed below.

The exponentially falling high-energy tail of the x-ray emission is characterized by a hot-electron temperature ( $T_h$ ) derived from the slope of the 20 to 50 keV region of the x-ray spectrum and by the total energy ( $E_{20}$ ) defined as the integrated x-ray flux above 20 keV. Values of  $T_h$  are presented in Fig. 10 as a function of the short-pulse laser energy (the corresponding vacuum intensity is shown at the top of the figure) for all three scalelengths. These temperatures range from 6 to 10 keV and have little dependence on laser energy. Average values at the three scalelengths are indicated in Fig. 10, and no more than a weak dependence on the scalelength is observed.

On the other hand, the intensity of the energetic x-ray emission, shown in Fig. 11, has several distinctive features in its dependence on short-pulse energy and plasma scalelength. Two thresholds are evident in the variation of  $E_{20}$ ; first, with increasing short-pulse energy at short scalelength and second, with increasing plasma scalelength at low short-pulse

energy (see Fig. 12). At short scalelength,  $E_{20}$  increases rapidly at an apparent threshold at  $\approx 5$  J corresponding to a vacuum irradiance of  $\approx 1 \times 10^{14}$  W/cm<sup>2</sup>. Above 20 J,  $E_{20}$  increases less rapidly in the short-scalelength plasma. At long scalelength, energetic x-rays are detected even for laser energies less than 5 J, so there is a threshold with increasing plasma scalelength for x-ray production at low incident energy. At higher energy (e.g., 20 J, corresponding to a vacuum intensity of  $5 \times 10^{14}$  W/cm<sup>2</sup>),  $E_{20}$  is nearly constant as the scalelength is increased; however, there is considerably more scatter in the measurements at longer scalelength and higher laser energy.

The fraction of laser energy deposited in hot electrons is evaluated from the measured energetic x-ray intensities and hot-electron temperatures. The fraction,  $f_h$ , is defined as the fraction of the incident laser energy ( $E_L$ ) which is contained in the entire Maxwellian distribution of the energetic electrons characterized by  $T_h$ . If one assumes that the high-energy x-ray spectrum is produced by thick-target bremsstrahlung<sup>52</sup> from electrons which impact the target and that one-half of the generated energetic electrons are directed into the target, one finds:

$$f_h = 1.43 E_{20} \text{ (ergs/sr)} / [E_L Z C(T_h)]$$

where  $C(T_h) = T_h [\exp(-20/T_h) - \exp(-50/T_h)]$ ,  $T_h$  is in keV, and  $Z$  is the atomic number of the target. For polystyrene targets in this experiment  $Z = 3.5$ .

Values of  $f_h$  are presented in Fig. 12 as a function of the scalelength at  $n_c/4$  since quarter-critical processes are a likely source of the energetic electrons (see next section). Results are presented for both high (20 J) and low (7 J) short-pulse energies. At high energy, the hot-electron fraction is not sensitive to the change in the preformed-plasma scalelength at  $n_c/4$ . Many speculative explanations may be offered for this observation, but at these higher energies the perturbation of the plasma by the short

pulse (Sec. V and Ref. 53) and the occurrence of self-focusing (Sec. V B and Ref. 46) greatly complicate the interpretation. Profile steepening in the underdense region may occur so that differences in scalelength that initially existed at  $n_c/4$  in the background plasma are no longer present. Also, at higher energy,  $n_c$  processes may be significant because more incident light reaches  $n_c$  in hotter plasmas. Further studies are required to identify the process(es) which generate suprathermal electrons at higher energy in these experiments.

At low energy (7 J), a threshold is apparent in Fig. 12 between the short and medium scalelength conditions. In contrast to the result at high energy, the hot-electron fraction increases with increasing scalelength at  $n_c/4$ , as one would expect if the hot electrons were due to a plasma instability at that density. Furthermore, the observations at low energy do not seem consistent with hot-electron production by processes at  $n_c$ . The scalelengths at  $n_c$  are calculated by the hydrocode to be nearly the same for the three focal conditions (an entirely reasonable result because the critical surface is too close to the target to be significantly affected by the 2-D expansion that is causing the scalelength variations in the underdense plasma further from the target). With constant scalelength, differences in hot-electron production at  $n_c$  should be due to changes in the amount of laser light that penetrates to that density. Less light reaches  $n_c$  in the long-scalelength plasma than in the short-scalelength plasma (22% vs. 53% according to hydrocode calculations), so one would expect fewer hot electrons to be generated at  $n_c$  with increasing scalelength. The measured variation is just the opposite and supports hot-electron production by an underdense process at low short-pulse energies.

## B. $3\omega_0/2$ DATA AND CORRELATION WITH X-RAY DATA

To test for hot-electron production by  $n_c/4$  instabilities, measurements correlating energetic x-rays with  $3\omega_0/2$  light were made for low short-pulse energies.<sup>45</sup> The  $3\omega_0/2$  light emitted in the plane of incidence at angles of  $30^\circ$  and  $45^\circ$  with respect to the laser axis ( $24^\circ$  and  $39^\circ$  relative to the target normal) was coupled to either filtered photodiodes to give good time resolution (0.35-nsec risetime) or to a spectrograph and optical multichannel analyzer (OMA) to give temporally integrated  $3\omega_0/2$  spectra. The observed duration of this emission is limited by detector risetime which indicates that the  $3\omega_0/2$  light is associated with the high-irradiance short laser pulse rather than with the low-irradiance 4-nsec pulse. Spectra of  $3\omega_0/2$  emission measured with the OMA are presented in Fig. 13. These spectra exhibit the characteristic two-peaked distribution (centered near  $3\omega_0/2$ ) that is usually attributed to processes involving plasma waves driven by the  $2\omega_p$  instability. Increased spectral broadening with increasing laser energy is apparent. For the photodiode detectors, the filter transmission is sufficiently broad to provide relative intensities of the  $3\omega_0/2$  emission without correcting for variations in the spectrum.

The results of these  $3\omega_0/2$  intensity measurements for short and long plasma scalelengths are compared with energetic x-ray measurements in Fig. 14. For short scalelength, a detection threshold for energetic x-rays is observed near 5 J; at this energy, the  $3\omega_0/2$  emission increases abruptly by more than an order of magnitude. Above 5 J, these radiations scale together with increasing laser energy and plasma scalelength. This positive correlation of  $3\omega_0/2$  with energetic x-ray intensities as both irradiance and scalelength are varied (a correlation with a two-dimensional parameter variation rather than the usual one dimension) supports suprathermal-

electron generation by a  $n_c/4$  process because  $3\omega_0/2$  emission is indicative of plasma density fluctuations near  $n_c/4$ .

### C. PLASMA INSTABILITIES AT QUARTER-CRITICAL DENSITY

Plasma instabilities which could drive plasma waves near  $n_c/4$  (and the resultant suprathermal electrons), are the convective Raman, the absolute Raman, and the  $2\omega_p$  processes. Growth rates and thresholds for these processes have been evaluated for the plasma conditions in this experiment. Both collisional and Landau damping, as well as the effect of inhomogeneity in the underdense region are included in these calculations.

For the convective Raman process, the number of e-foldings in intensity is given by:<sup>54,55</sup>

$$N_e = 2\pi\gamma_0^2 / (V_s V_L K')$$

where the homogeneous growth rate  $\gamma_0$  is

$$\gamma_0 = k_L v_0 / 4(\omega_p / \omega_s)^{1/2},$$

and the mismatch  $K'$  is

$$K' = \omega_p^2 / (2L_n) \times [-1/(k_0 c^2) + 1/(k_{s,x} c^2) + 1/(3k_{L,x} c^2)]$$

The group velocities  $V_s = c^2 k_s / \omega_s$  and  $V_L = 3 v_e^2 k_L / \omega_L$  correspond to the scattered and Langmuir waves with wave number (frequency) values of  $k_s(\omega_s)$  and  $k_L(\omega_L)$ , respectively. The laser is incident from the  $+x$  direction with wave number  $k_0$  in the plasma and produces an electron quiver velocity  $v_0$  in the plasma. The value of  $v_0$  in this paper is twice the value of  $v_0$  in refs. [54, 55, and 59]. For a laser of wavelength  $\lambda_0$  in  $\mu\text{m}$  and with irradiance  $I$

in  $W/cm^2$ ,  $v_o = 25.6\lambda_o^{-1/2}$  in  $cm/s$ . The plasma frequency is  $\omega_p = v_e/\lambda_D$ , and the electron thermal speed is  $v_e = (T_e/m)^{1/2}$ .

For the longest scalelength ( $L_n = 320 \mu m$ ) and for an irradiance of  $10^{14} W/cm^2$ , we find the number of convective Raman e-foldings  $N_{SRS} < 0.9$  in the underdense region where  $0.05 < n/n_c < 0.240$ . For smaller values of  $n/n_c$ , the Langmuir waves are strongly Landau damped. As the density approaches  $n_c/4$ , the evaluation of  $N_{SRS}$  by the WKB approximation fails,<sup>56</sup> and these plasma waves are trapped at  $n_c/4$ .<sup>57</sup> A condition for the breakdown of the WKB approximation<sup>58</sup> is reached in this experiment for  $n/n_c = 0.0245$ , but for  $n/n_c < 0.240$ ,  $N_{SRS}$  is at least a factor of three less than the value at the WKB limit. We conclude that convective Raman is unlikely in this experiment because less than one e-folding of growth is predicted at  $10^{14} W/cm^2$  (the irradiance at 5 J if there is no self-focusing) in the region below  $0.24n_c$ .

For the absolute Raman and  $2\omega_p$  processes, the following expressions were used to evaluate growth rates for the plasma wave amplitudes generated by the instabilities:

Absolute Raman:<sup>54,55</sup>

$$\Gamma_R = (\pi v_c/\lambda_o) (3^{1/2})/4 [1 - 1/(3^{1/4} k_o L_n) (v_o/c)^{-3/2}] - (\gamma_L + v_c/2)$$

Two Plasmon Decay:<sup>59-61</sup>

$$\Gamma_{2\omega_p} = k_o v_o/4 [1 - 3^{3/2} k_y v_e^2/(2 v_o \omega_p)] - \omega_p/(4 k_y L_n) - (\gamma_L + v_c/2)_{rms}$$

where  $k_y$  is the transverse momentum of the plasma waves. The coefficient  $3^{3/2}/2$  in the second term of this expression corrects an error in ref. 60 (see the linear fit in Fig. 4-44 of this reference). Also, the

inhomogeneous term has been modified to correspond to the definition of  $L_n$  in this paper. To account phenomenologically for damping, the rates for Landau damping<sup>62</sup> ( $\gamma_L$ ) and electron-ion collisional damping<sup>63</sup> ( $\nu_c$ ) are subtracted from these growth rate expressions. For the  $2\omega_p$  process, two plasma waves are generated; the total damping rate for each wave is taken to be the sum of the Landau and collisional damping rates and the rms value of the total damping rate for the two waves is used to evaluate the growth rate.<sup>54</sup>

Thresholds (zero growth rate) and growth rates at  $10^{14}$  W/cm<sup>2</sup> (the irradiance at 4 J if there is no self-focusing) are listed in Table I for these processes. For the  $2\omega_p$  process, a plasma temperature of 600 eV near  $n_c/4$  is taken from the hydrodynamic calculations for this short-pulse energy. The calculated growth rates at long scalelength for both instabilities and at short scalelength for the  $2\omega_p$  instability allow several e-foldings of growth during the 300-psec laser pulse. The lower thresholds and faster growth rates for the  $2\omega_p$  instability suggest that this process is the more likely source of suprathermal electrons in this experiment, at least at low short-pulse energy. Furthermore, this instability most easily accounts for the double-peaked  $3\omega_0/2$  spectra.

The measured values of the hot-electron temperature are significantly less than temperatures associated with electrons trapped in the most unstable plasma waves associated with these instabilities. Calculated values of  $I\lambda_p^2$  at threshold for the  $2\omega_p$  process are presented in Fig. 15 in terms of the wave number  $k_y$  transverse to the direction of laser propagation. The plasma waves are strongly damped at the larger  $k_y$  values, predominantly by Landau damping. The minima of the curves for  $L_n = 140 \mu\text{m}$  (short scalelength) and  $L_n = 320 \mu\text{m}$  (long scalelength) correspond to the threshold values in Table I for two-plasmon decay. These most unstable

waves correspond to  $k_y \lambda_D \approx 0.02$  for both short and long scalelength plasmas. Using the  $\omega$ - and  $k$ -matching relations for the three waves of the  $2\omega_p$  instability and for the conditions of this experiment, we find with this transverse momentum that the two plasma waves have  $k\lambda_D \approx 0.07$  and  $k\lambda_D \approx 0.02$ . If the hot-electron temperature is given by the energy associated with the phase velocity  $v_{ph}$  of the most unstable waves, then the plasma-wave dispersion relations give:

$$T_h = mv_{ph}^2/2 = T_e [3 + (k\lambda_D)^{-2}]$$

where  $T_e$  is the plasma thermal temperature. For the larger  $k\lambda_D$  value and  $T_e = 600$  eV (at  $k_y = 0$ ), Eq. 4 implies  $T_h > 100$  keV, which is more than an order of magnitude larger than the measured values of  $T_h$  (see Fig. 10). The measured hot-electron temperatures correspond to plasma waves with  $k\lambda_D \approx 0.25$  to 0.4, which are strongly damped and therefore less likely to be unstable.

## V. PERTURBATIONS TO THE PLASMA AND SELF-FOCUSING

### A. Temperature Perturbations

Perturbations to the background plasma by the 300-psec, high-irradiance laser beam are not completely eliminated by using a short pulse-duration; additional plasma heating does result from the high intensity of this pulse. Temperatures of the background-plasmas that are heated by the long pulse only and temperatures of the perturbed-plasmas that are heated by both laser pulses are determined by time-resolved measurements of the thermal x-ray emission. Two detectors are used, with K-edge filters that are designed to

Table I            Thresholds and Growth Rates at  $10^{14}$  W/cm<sup>2</sup> for  
Underdense Plasma Instabilities.

Instability	Short Scalelength		Long Scalelength	
	Threshold ( $10^{14}$ W/cm <sup>2</sup> )	Growth Rate ( $10^{12}$ sec <sup>-1</sup> )	Threshold ( $10^{14}$ W/cm <sup>2</sup> )	Growth Rate ( $10^{12}$ sec <sup>-1</sup> )
Absolute Raman	1.6	stable	0.63	0.96
Two-Plasmon Decay	0.46	1.2	0.26	1.3

detect 1 to 1.5 keV and 2 to 2.8 keV photons, respectively. Measurements with identical filters on these two detectors are made to correct for different detector sensitivities. Each detector consists of a 1.6-mm thick quenched (3% benzophenone) plastic scintillator<sup>67</sup> coupled to a vacuum photodiode giving an overall response time  $\approx 0.7$  nsec. Oscilloscope traces for these two detectors (Fig. 16) show a subnanosecond radiation spike, associated with the short laser pulse, occurring near the peak of the longer duration x-ray pulse that is associated with the long laser pulse. X rays from the long pulse are time-resolved, but the short pulse is time-integrated by the detector. For a Maxwellian electron-energy distribution, temperatures may be determined from the two detector signals because the ratio of the signals is a strong function of plasma temperature for temperatures  $< 700$  eV. Background-plasma temperatures, evaluated at maximum x-ray emission of the long pulse, are 310, 350, and 370 eV for the short,

One possible explanation for the measured small  $T_h$ -values is that the transfer of energy from the plasma waves to the electrons may be preceded by wave energy cascading from the  $2\omega_p$  driven, small- $k$  modes (which are weakly damped) to the larger- $k$  modes which are more strongly coupled to the electrons by Landau damping. This process has been predicted theoretically<sup>64</sup> and has been observed in computer simulations of the  $2\omega_p$  and Raman instabilities.<sup>65</sup> Experimental evidence has also been obtained for ion waves that may cause this mode-coupling of electron plasma waves.<sup>66</sup> medium, and long scalelength conditions, respectively. These values represent averages over 6-7 shots where the shot-to-shot variation is  $\leq 10\%$ . These temperatures are consistently higher than the time-integrated measurements (see Sec. IV), as one intuitively expects. Perturbed plasma temperatures, determined from ratios of the peaks of the short x-ray pulses, are plotted in Fig. 17 as a function of the short-pulse

energy and vacuum intensity for the three scalelength conditions. The time-resolved background-plasma temperatures are displayed as dashed lines for comparison. These results indicate that, on the average, the plasma thermal temperature is increased by 30-40% due to the high-irradiance short pulse. Because these detectors integrate the short x-ray pulse, the perturbed-plasma temperatures represent lower limits on the plasma heating; the temperature increase may be larger than indicated by these measurements.

Hydrodynamic simulations of the experimental conditions are also used to assess perturbations to the plasma by the short-pulse beam. For these simulations, temporally and azimuthally averaged radial beam profiles of the two incident laser pulses, based on experimental measurements,<sup>68</sup> are used.

The simulations provide temperature and density profiles of the target plasmas as a function of time during the laser pulses. These profiles are used to calculate free-bound x-ray radiation spectra for comparison with the experimental measurements. Temperatures are derived from the slopes of the calculated x-ray spectra in the 1 to 3 keV region. Background-plasma temperatures are computed from spatially averaged instantaneous spectra at the peak of the long laser pulse; the condition corresponding to the time-resolved, background-plasma temperature measurements. Calculated temperatures for the short and long scalelength plasmas are 360 and 405 eV, respectively; which are 10-15% higher than the measured background-plasma temperatures. Perturbed-plasma temperatures are computed from x-ray spectra which are integrated spatially over the entire plasma (but subtracting out the contribution of the long pulse using a separate computer run with no short pulse) and temporally over the short pulse duration; the condition corresponding to the perturbed-plasma temperature measurements. Calculated temperatures for short-pulse energies of 5 J and 25 J, for short and long plasma scalelengths are shown in Fig. 17. The calculated temperatures are

consistently higher than the experimental values, but calculated ratios of the temperature increase due to perturbation by the short pulse are in good agreement with the ratios based on the measured temperatures. The larger calculated temperatures may be due to the fact that refraction of the incident laser beam in the underdense region is not included in the calculations. Only a small amount of refraction would be required to increase the heated target area by the 10% needed to explain the discrepancy.

#### B. Density Perturbations and Self-focusing

The hydro-code predicts two types of density perturbations that result from the higher-intensity short pulse. At the higher pulse energies, an axial shock propagates down the background density gradient, driven by the increased mass ablation rate due to the higher incident intensity. In Fig. 18 is shown the temporal evolution of the axial density and velocity profiles for a case with 25 J of energy in the short pulse incident upon a long-scalelength background plasma. Note the rather large perturbations of the density and velocity scalelengths near  $n_c/4$  at a time shortly after the peak of the short pulse. The location of this shock temporally and spatially is sensitive to the details of the experimental conditions. It may explain in part the increased scatter in the energetic x-ray intensities at higher short-pulse energies (see Fig. 11) as well as the falloff in backscatter reflectivity (see Sec. III B). A second type of density perturbation results from the radial pressure imbalance caused by localized heating in the high intensity channel. Shown in Fig. 19 are radial density and temperature profiles predicted by the hydrodynamic simulations at two axial locations: one near  $n_c/4$  and the other near  $n_c/10$ . Four cases are represented near the extremes of the experimental conditions: namely low (5 J) and high (25 J) short pulse energies and short and long background-

plasma scalelengths. The on-axis density depression  $\Delta n/n$  increases with both increasing energy and increasing scalelength, ranging from a negligible level at low energy and short scalelength to nearly 15% at  $n_c/4$  for the 25 J, long-scalelength case. It should be emphasized that these calculations do not include laser beam refraction (self-focusing) due to these plasma density perturbations; therefore, these calculations probably underestimate the actual perturbations, and they serve mainly as a guide to the potential for induced radial perturbations.

Time-integrated, spatially resolved images of second-harmonic ( $2\omega_0$ ) emission can provide experimental evidence for such plasma perturbations and for self-focusing at the higher incident laser intensities.<sup>46</sup> Light emitted from the plasma parallel to the target is collected and collimated with an f/2.8, 10-cm focal-length lens, then imaged onto film with a 50 cm lens to produce a recorded magnification of 5. A narrow-bandpass interference filter (12-Å FWHM) is used to select the second-harmonic wavelength (527 nm). A Wollaston prism is used on some shots to obtain two separate images of the orthogonally polarized  $2\omega_0$  light.

A threshold is observed where the patterns of  $2\omega_0$  emission change dramatically. At low short pulse energies corresponding to vacuum intensities  $< 3 \times 10^{14} \text{ W/cm}^2$ , a large region of weak  $2\omega_0$  emission is observed in the region corresponding to the  $\approx 1 \text{ mm}$  spot diameter of the long pulse beam. This is primarily plasma continuum radiation that falls into the bandpass of the filter. There is an additional region of emission between the  $n_c$  and  $n_c/4$  density region with transverse dimension comparable to that of the high-intensity beam. This is primarily  $2\omega_0$  emission as verified by filter substitution at nearby wavelengths. There is no evidence in the lower-intensity shots that the background plasmas are appreciably perturbed.

At higher intensities ( $>3 \times 10^{14} \text{ W/cm}^2$ ), in addition to the unpolarized light from the  $n_c$  to  $n_c/4$  region, intense filamentary structures (polarized normal to the direction of laser beam propagation) appear far from the target surface (up to  $\approx 1 \text{ mm}$ ), corresponding to background-plasma densities between 0.01 and 0.1  $n_c$ . These often appear as multiple bursts of about 100  $\mu\text{m}$  length and  $< 5 \mu\text{m}$  diameter. The polarization of the emission from the region far from the target is consistent with second-harmonic emission produced by an electric field vector oscillating along a radial density gradient, as expected if a density channel existed along the laser axis; this is in contrast to the polarization observed for the light from the higher density region which is more consistent with an electric field oscillating along a density gradient parallel to the laser axis.

The distance from the target at which the filamentary structures first appear increases with the scalelength of the preformed plasma. Furthermore, the background-plasma density corresponding to this distance also decreases with increasing scalelength (from  $0.08 n_c$  in the long-scalelength plasma to  $0.2 n_c$  at short-background scalelength. All of these  $2\omega_0$  observations are consistent with self-focusing of the incident laser beam in the underdense region, which can result from the creation of a density channel along the laser axis.

Theoretical estimates and computer simulations support the interpretation of self-focusing of the high-intensity laser beam. A steady-state treatment of self-focusing, including ponderomotive and thermal terms, shows that under the conditions of this experiment: 1) the convective growth lengths are indeed short enough to allow significant filamentation, and 2) the ponderomotive term dominates the thermal term in the far underdense plasma.<sup>46</sup> The calculations support the experimental observations that: 1)

the self-focusing occurs at a very low plasma density ( $n < 0.1 n_c$ ) in the long-scalelength plasma, 2) the distance from the target at which the beam self-focuses increases with plasma scalelength and 3) the density at which self-focusing occurs decreases with increasing plasma scalelength. The production of second-harmonic emission in these very underdense filaments has been explained by a theoretical model involving the interaction of the incident laser beam with reflected or backscattered light.<sup>46</sup> While the observed trend toward increased self-focusing at lower densities for longer scalelengths is somewhat troubling for laser fusion, it must be remembered that this experiment is particularly susceptible to self-focusing due to the low plasma temperatures and small focal spot sizes with strong radial gradients.

## VI. SUMMARY AND CONCLUSIONS

In this paper we describe a new technique for simultaneously generating high intensities and long-scalelength plasmas which are of interest for absorption studies relevant to high-gain systems. It involves the use of a two-beam system where a high-intensity, short-pulse beam is tightly focused onto a long-scalelength preformed background plasma generated by a large focal diameter, long-duration, low-intensity beam. For a given laser energy, this method allows the production of a much longer plasma scalelength than is possible with a single beam at high intensity. An additional advantage of such a system is that it allows independent control of the incident intensity and plasma scalelength. It also allows more independent control of plasma temperature than with a single beam.

The new technique also has some drawbacks. One disadvantage is that the plasma temperatures are lower than those anticipated for high-gain laser fusion. There are two other inherent limitations: 1) The limited diameter of the high intensity beam may prevent adequate simulation of plasma instabilities (e.g. Brillouin sidescatter) that require a large transverse scalelength, and 2) the high intensity beam may perturb the long-scalelength background plasma, clouding the interpretation of the results and making extrapolation to high-gain systems difficult.

These difficulties can be overcome somewhat by increased laser energy. With more energy the spot size of the high-intensity beam can be increased. This increases the radial scalelengths to allow transverse growth of plasma instabilities and reduces the lateral gradients that drive the radial perturbations. The axial plasma perturbations are somewhat more difficult to control. Basically, there are two competing effects. Reducing the the pulse length of the high-intensity beam will reduce the effect of the axial shock wave if the high-intensity interaction is completed before the axial shock reaches the underdense region. On the other hand, shortening the pulse duration might also limit the growth of some plasma instabilities of interest.

These experiments provide the first direct measurements of the variation with plasma scalelength of absorption phenomena important to high-gain systems; however, extrapolation of these results to high-gain systems must be done with some care. The results that are most relevant to high-gain systems are: 1) the limitation of absorption by backscatter at longer scalelength, 2) the increased production of energetic electrons at longer scalelength, and 3) the onset of self-focusing. The scaling of each of these results is discussed below:

## 1) Absorption

If we restrict ourselves to low incident energies where the effects of plasma perturbations are expected to be minimal, the results of the scattered light measurements outside the focal cone indicate that collisional absorption becomes increasingly effective at longer scalelengths. At the same time, the levels of backscatter are found to increase at longer scalelengths (at mid  $10^{14}$  W/cm<sup>2</sup> backscatter reaches >20% for the longest scalelength). In Appendix I, this observed variation of backscatter with scalelength is seen to agree with linear SBS theory if the noise source for the instability is specularly reflected light, which decreases with increasing scalelength. At the longest scalelength of this experiment, collisional absorption nearly saturates and the increased backscatter limits the overall absorption. As pointed out in the Appendix and in Secs. III B and III D, the exact levels of backscatter in a high-gain system also depend upon instability noise levels, which may be very different from those of the experiment. Nevertheless, the increase of backscatter with scalelength that is observed in this experiment, coupled with the agreement with SBS theory, raises serious concern that a narrow-bandwidth, 1  $\mu$ m laser system will have unacceptably high levels of backscatter at the much longer scalelength of a high-gain system.

## 2) Energetic Electrons

The correlation of energetic x rays and  $3\omega_0/2$  light provides evidence for the production of energetic electrons in the underdense region near  $n_c/4$ . This is important for laser fusion because laser light is expected to reach the  $n_c/4$  region even for the longer scalelengths associated with high-gain systems. If the energetic electrons were produced near the critical surface as in many short-scalelength experiments, they would be of less concern; in the longer scalelengths of high-gain systems, only a small

percentage of the incident laser light is expected to reach the critical surface.

Evidence for two thresholds for the onset of hot-electron production is found, one with increasing plasma scalelength at low laser intensity and another with increasing intensity at short plasma scalelength. While the level of energetic electron production is of some concern, direct extrapolation of the levels and temperatures of the hot electrons to high-gain systems is difficult because the scaling laws are not well known. However, these results provide valuable benchmarks for theoretical or computational models that are used for scaling to high gain systems.

### 3) Self-focusing

Evidence for self-focusing in the far underdense plasma ( $n < 0.1 n_c$ ) is found in filamentary emission of  $2\omega_0$  light far from the target surface. This result is not directly scalable to high-gain systems because this particular experiment is highly susceptible to self-focusing due to the strong radial perturbations of the plasma. The high energy beam in effect acts like a hot spot in a colder background beam; at the highest short-pulse intensities, this hot spot represents a 100:1 intensity modulation over the background-intensity, far more than the few percent envisioned for high-gain laser fusion. However, the results of this experiment have demonstrated  $2\omega_0$  light as a diagnostic for detection of self-focusing. Moreover, the good agreement between the computational model for self-focusing and the experiment<sup>46</sup> gives some confidence in the ability of present theory to predict self-focusing in high-gain systems.

The results of this experiment indicate that narrow-bandwidth 1  $\mu\text{m}$  laser light is very likely to have considerable difficulties as a driver for high-gain systems due to reduced absorption efficiency and increased energetic electron production at longer plasma scalelengths. Hopefully,

proposed mechanisms such as shorter laser wavelength and wider laser bandwidth will be sufficient to control the plasma instabilities that cause these absorption difficulties.

## VII. ACKNOWLEDGMENTS

The authors wish to acknowledge valuable conversations with R.H. Lehmberg, A.J. Schmitt, S.E. Bodner, W.L. Kruer, A.B. Langdon, B.F. Lasinski, B.H. Ripin, and E.A. McLean. One of us (JHG) wishes to acknowledge the development of the 2-D hydro-code by J.P. Boris and M.E. Emery. We also appreciate the technical assistance of L. Daniels, M. Fink, J. Kosakowski, N. Nocerino, V. Salzmann, and E. Turbyfill. This work was supported by the U.S. Department of Energy and the Office of Naval Research.

## APPENDIX I. Brillouin Backscatter Calculation

As discussed in Sec. III B, a simple model for calculating Brillouin backscatter reflectivity is constructed in order to determine whether the observed increase of reflectivity at long scalelength is consistent with SBS. The reflectivity  $R$  varies as<sup>69</sup>

$$R(1-R) = B \exp[N(1-R) - R] \quad (1)$$

where  $B$  is the noise level from which the backscatter grows and  $N$  is the number of linear e-foldings of the instability. In an inhomogeneous plasma,  $N$  is a function of the resonant density where the frequencies  $\omega$  and the wave vectors  $k$  of the three waves in the instability are matched:

$$\omega_o = \omega_L + \omega_s \quad (2A)$$

$$k_o = -k_L + k_s \quad (2B)$$

The subscripts  $o$ ,  $L$ , and  $s$  refer to the incident electromagnetic wave, the scattered light wave, and the excited sound wave, respectively (in this discussion the  $k$ 's are magnitudes and the signs for backscatter are given explicitly). As the waves propagate away from the resonance point, the  $k$ 's change according to the lab-frame dispersion relations for the three waves:

$$\omega_{o,L}^2 = \omega_p^2 + k_{o,L}^2 c^2 \quad (3A)$$

$$\omega_s = -k_s u + k_s c_s / (1 + k_s^2 \lambda_D^2)^{1/2} \quad (3B)$$

where  $\omega_p$  is the spatially varying plasma frequency,  $c$  is the speed of light in vacuum, and  $u$  is the spatially varying flow velocity. The displayed sign corresponds to a flow velocity that is antiparallel to  $k_s$ , as appropriate for the experiment. The Debye length  $\lambda_D = v_e/\omega_p$  where  $v_e = (T_e/n)^{1/2}$  is the thermal speed of the electrons at temperature  $T_e$ . The acoustic speed is  $c_s = [(ZT_e + 3T_i)/M]^{1/2}$  for ions of charge  $Z$ , temperature  $T_i$  (assumed to be equal to  $T_e$  in our calculations), and mass  $M$ . As the  $k$ 's change according to Eq. 3 with distance  $z$  from the resonance point, a mismatch  $K = k_o + k_L - k_s$  develops, reducing the Brillouin gain from its value at resonance. If the mismatch  $K$  varies linearly with  $z$ ,<sup>10</sup> the growth region around the resonance point  $z = z_o$  extends from  $-z_T$  to  $+z_T$  where the turning point  $z_T = (1/K') [2\gamma_o/(v_s v_L)^{1/2} + \Gamma_s/v_s]$ . Here  $\Gamma_s$  is the damping rate for the sound wave (taken to be 0.1  $W_s$  for this calculation),  $v_s = -u + c_s/(1+k_s^2\lambda_D^2)^{3/2}$  and  $v_L = c(1-n/n_c)^{1/2}$  are the group velocities of the sound and backscattered waves, and  $K' = dK/dz$  is the rate of change of the linear mismatch. The homogeneous SBS growth rate  $\gamma_o = (2^{-3/2} v_s/c)\omega_{pi} (c/c_s)^{1/2} (ck_c/\omega_o)^{1/2}$  where  $\omega_{pi}$  is the ion plasma frequency. The number of linear SBS e-foldings within the resonance region  $-z_T < (z-z_o) < +z_T$  is given by<sup>10</sup>

$$N = 2\pi \gamma_o^2 / (K' v_L v_s) \quad (4)$$

The number of e-foldings is independent of  $\gamma_s$ ; the decrease in the SBS gain at the resonance point  $z_o$  is exactly offset by the increase in the width  $2z_T$  of the resonance region. By differentiating Eqs. 3 with respect to  $z$ , an expression for  $K'$  is obtained<sup>11</sup>

$$K' = d(k_o + k_L + k_s)/dz = [(n/n_c)k_o/(1-n/n_c)^{1/2} k_s^2 \lambda_D^2, 2MADE_L n + k_s/2L_u - k_s/2MADE_T]$$

In order to calculate  $N$ , a resonant density  $n_{res}$  is selected and the temperature  $T$ , the velocity  $u$ , and the scalelengths  $L_n$ ,  $L_m$ , and  $L_u$  are determined from the hydrodynamics calculation. A case with 5 J in the short pulse is chosen so as to avoid uncertainties raised by the severe plasma perturbations and self-focusing at higher energies. The number of linear e-foldings is then determined from Eqs. (4) and (5). In calculating  $N$ , the incident intensity is assumed to be constant within the interaction region. This constant value is the intensity, reduced by collisional absorption, that penetrates to the resonant point in the hydrodynamic calculation. Because of the large depth of focus of the incident beam, no intensity adjustment is required for beam convergence within the resonance region. As a final step, the linearity of  $K$  is checked within the resonant region; in all cases, the linear mismatch approximation appears to be justified. In the few cases with the most nonlinear  $K$ 's, the linear-mismatch assumption is checked further by calculating the SBS growth with a model in which the gain  $\gamma(z)$  is allowed to vary according to the local value of  $K$ ; in even the worst cases, the number of e-foldings within the interaction region was within 10% of the linear-mismatch model.

By varying  $n_{res}$ , the optimal region for Brillouin growth is identified. For the short-scalelength plasma with 5 J incident in the short pulse, 6.6 linear e-foldings of Brillouin growth are predicted at the optimal resonant density of  $0.4 n_c$  (with the growth region spanning  $0.35 n_c < n < 0.45 n_c$  for  $\Gamma_s/\omega_s = 0.1$ ). The model predicts 10.9 linear e-foldings in the long-scalelength case, 65% greater than the number for the short scalelength case. The optimal resonance region is centered at  $0.3 n_c$  and extends from  $0.27 n_c$  to  $0.33 n_c$ .

While the number of linear e-folds nearly doubles in the long-scalelength case, as expected, the comparison of Eq. (1) and the observed data depends upon the noise level  $B$  as well as upon the number  $N$  of e-folds. For this calculation it is assumed that the noise source for SBS growth is incident light that penetrates to the critical surface and is specularly reflected.<sup>73,74</sup> Given the experimentally inferred angular distribution of light reflected outside the incident lens (Fig. 5A), the fraction of the total specular light that is reflected back into the lens cone is found to be 0.25% by integration over the solid angle subtended by the lens. The total specular scatter with 5 J incident is seen from Figs. 5B and 5D to be about 5% for the short-scalelength plasma and 0.5% for the long-scalelength plasma. Thus, the level of this noise source is  $1.25 \times 10^{-4}$  for the short-scalelength plasma. The increased collisional absorption in the long-scalelength plasma reduces this noise source by an order of magnitude below the level for the short-scalelength plasma.

If specular reflection provides the noise source for SBS, the number of linear e-folds must be taken near the Mach-one region,<sup>73,74</sup> rather than the region of optimal gain. With a nearly stationary critical surface where  $A = (1 + k_s^2 \lambda_D^2)^{3/2}$ ,  $D = 1 - (1/MA)$ , and the mach number  $M = u/c_s$ . The scalelengths  $L_n$ ,  $L_T$ ,  $L_u$ , for the density, temperature, and velocity have a sign as well as a magnitude; for example  $L_n = n/(dn/dz) < 0$  if  $dn/dz < 0$ . (predicted by the hydrocode due to the long pulse used to establish the density profile), the specular light in the lab frame has almost no Doppler shift from the incident laser frequency. The frequency matching condition for SBS (Eq. 2A) then requires that the lab frame acoustic frequency (Eq. 3B) vanish. This happens when the Mach number  $M = (1 + k_s^2 \lambda_D^2)^{1/2}$  near the Mach-one point. Fortunately, the region of optimal SBS growth found for

the short-scalelength plasma is in this same region. In the long-scalelength plasma, however, the matching condition with specular light occurs at  $n_{res} = 0.25 n_c$  where the calculated number of e-folds  $N = 10.2$ , rather than the 10.9 found above for the optimal resonant density.

A comparison is now made between the calculated number of e-folds and the number required by Eq. (1) to produce the observed reflectivity with the observed specular noise levels. For the short-scalelength plasma with the observed reflectivity of 5.5%, Eq. (1) yields 6.4 linear e-folds which is well within the estimated 10% uncertainty of the calculated 6.6 e-folds. Similarly, with the reduced noise level at long-scalelength, Eq. (1) requires 9.4 e-folds to give the 8% reflectivity of Fig. 6C at 5 J incident, within 10% of the calculated value of 10.2 e-folds. This agreement proves neither that the backscatter is due to SBS nor that specular reflection is the noise source; however, the calculation does show that the observations are consistent with both of these hypotheses.

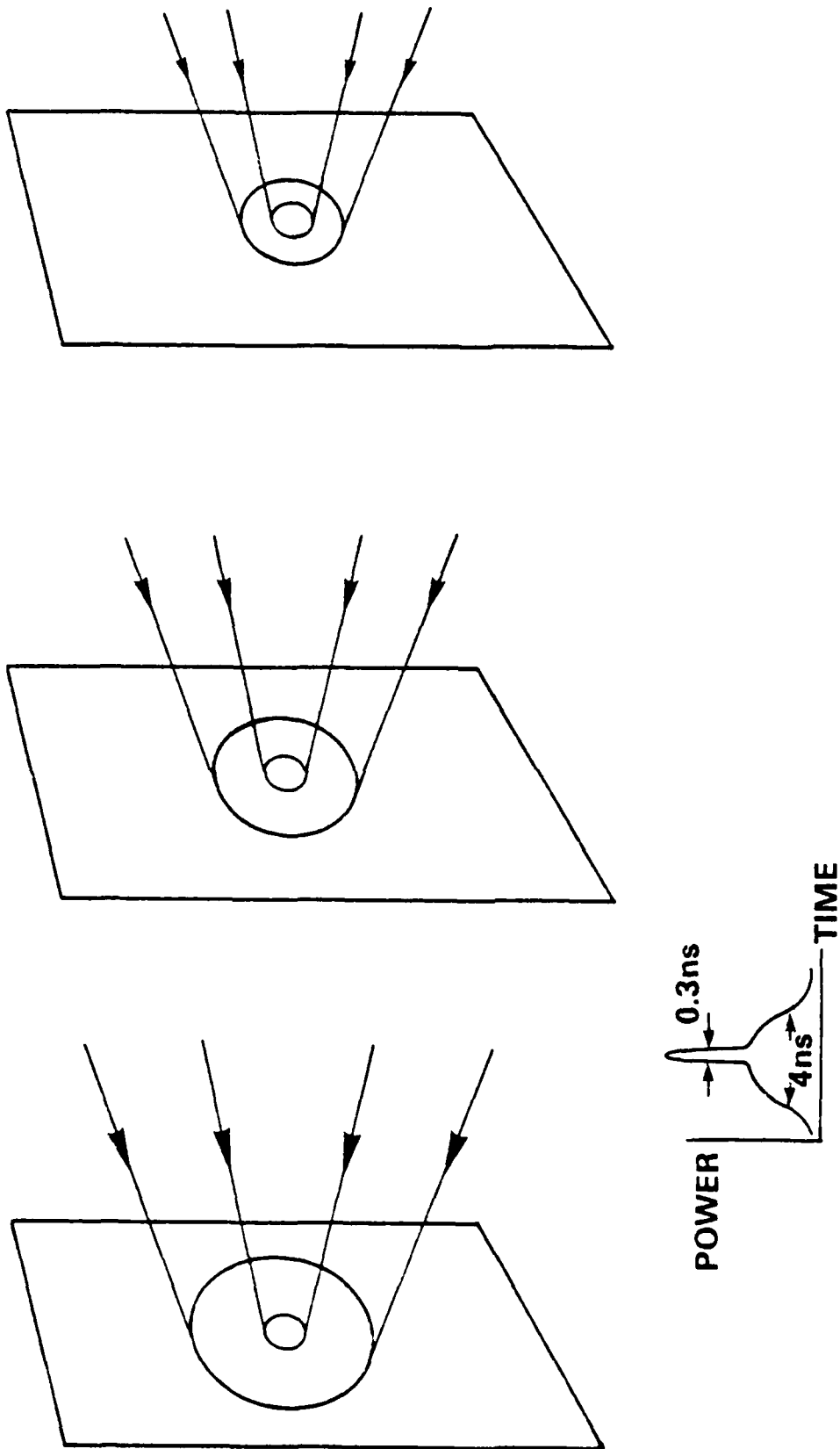


Fig. 1 Schematic picture of the laser beam arrangement for the controlled plasma scalelength experiments. The long-pulse defocused beam is apertured to three successively smaller radii to vary the plasma scalelength. A short pulse synchronized to the peak of the long pulse and tightly focused at the center of the defocused beam provides the high intensity for interaction studies.

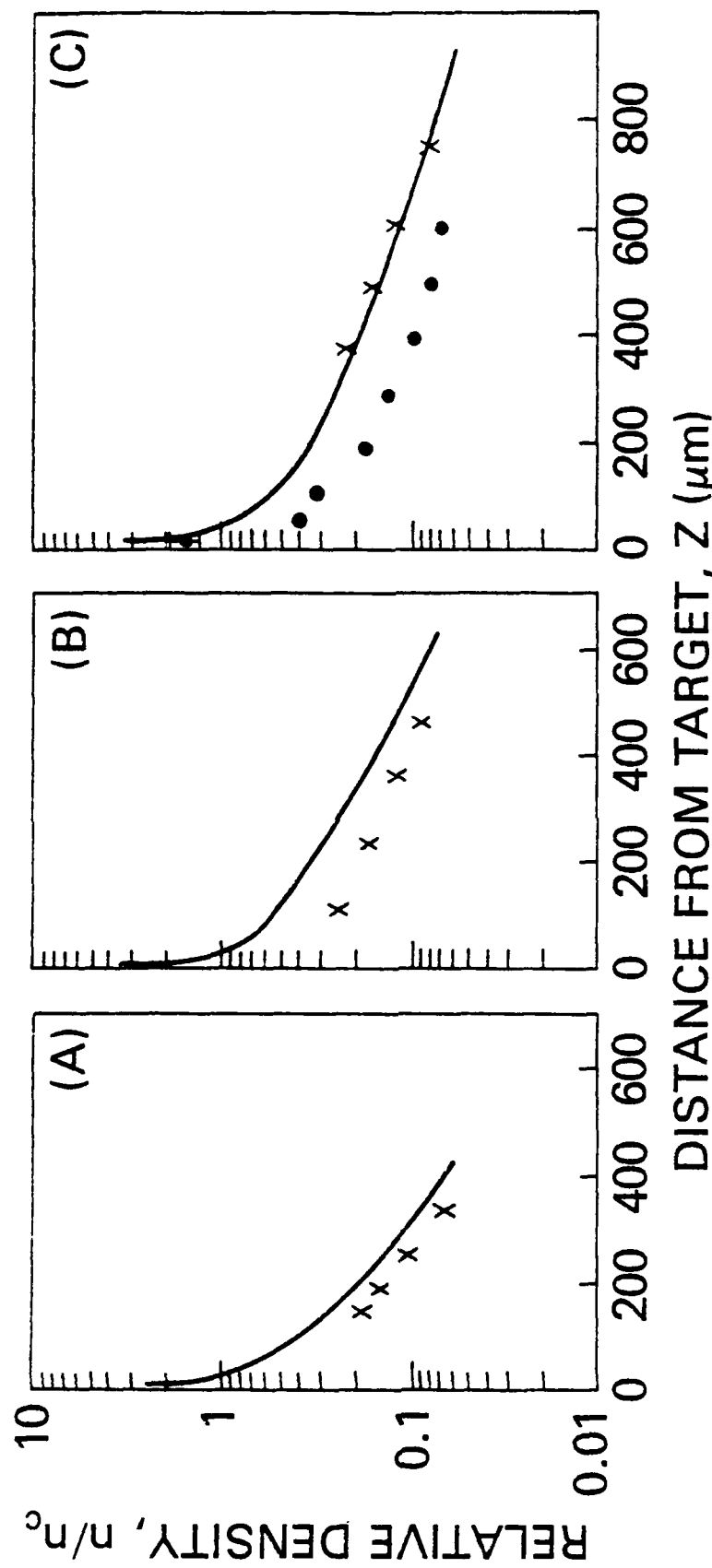


Fig. 2 Density along the axis normal to the target surface for the (A) short, (B) medium, and (C) long-scalelength background plasmas. Solid lines are hydrodynamic calculation results, the 'x's are interferometric data and the solid points are spectroscopic data.

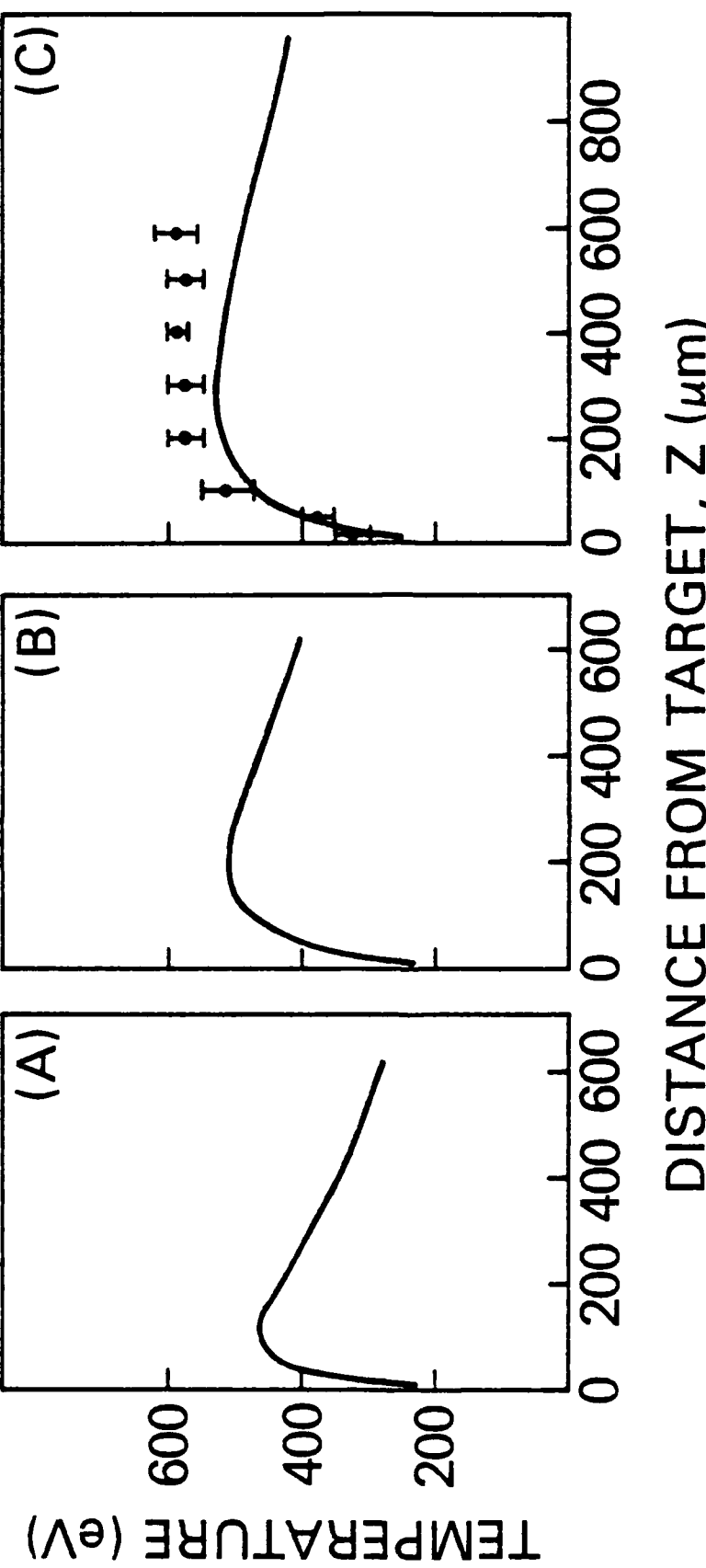


Fig. 3 Temperatures along the axis normal to the target surface for the same scalelength conditions as Fig. 1. The solid lines are hydrodynamic calculation results and the data points are from spectroscopic data.

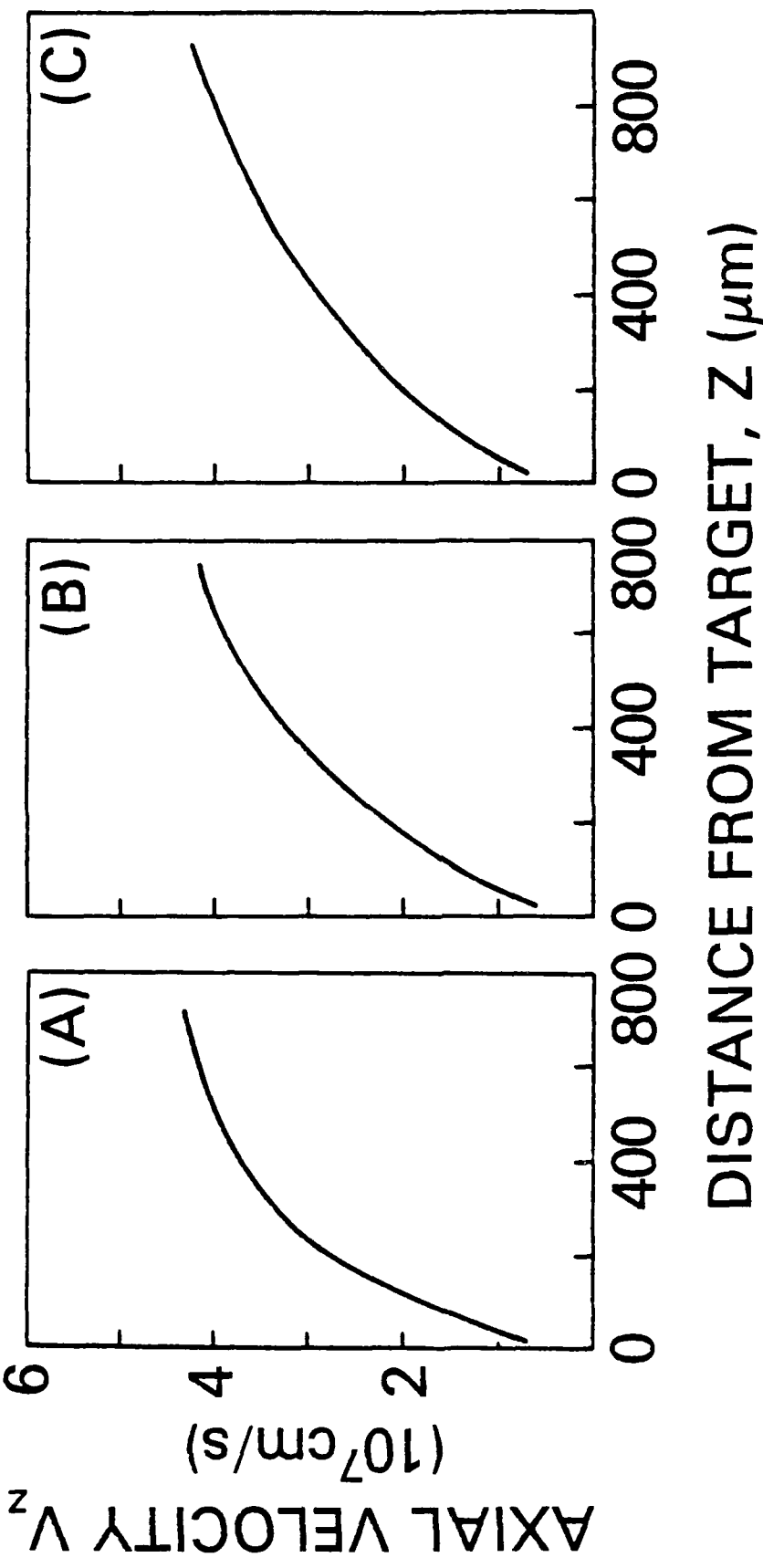


Fig. 4 Axial fluid velocity as a function of distance along the axis normal to the target from hydrodynamic calculations for (A) short, (B) medium, and (C) long-scalelength background plasmas.

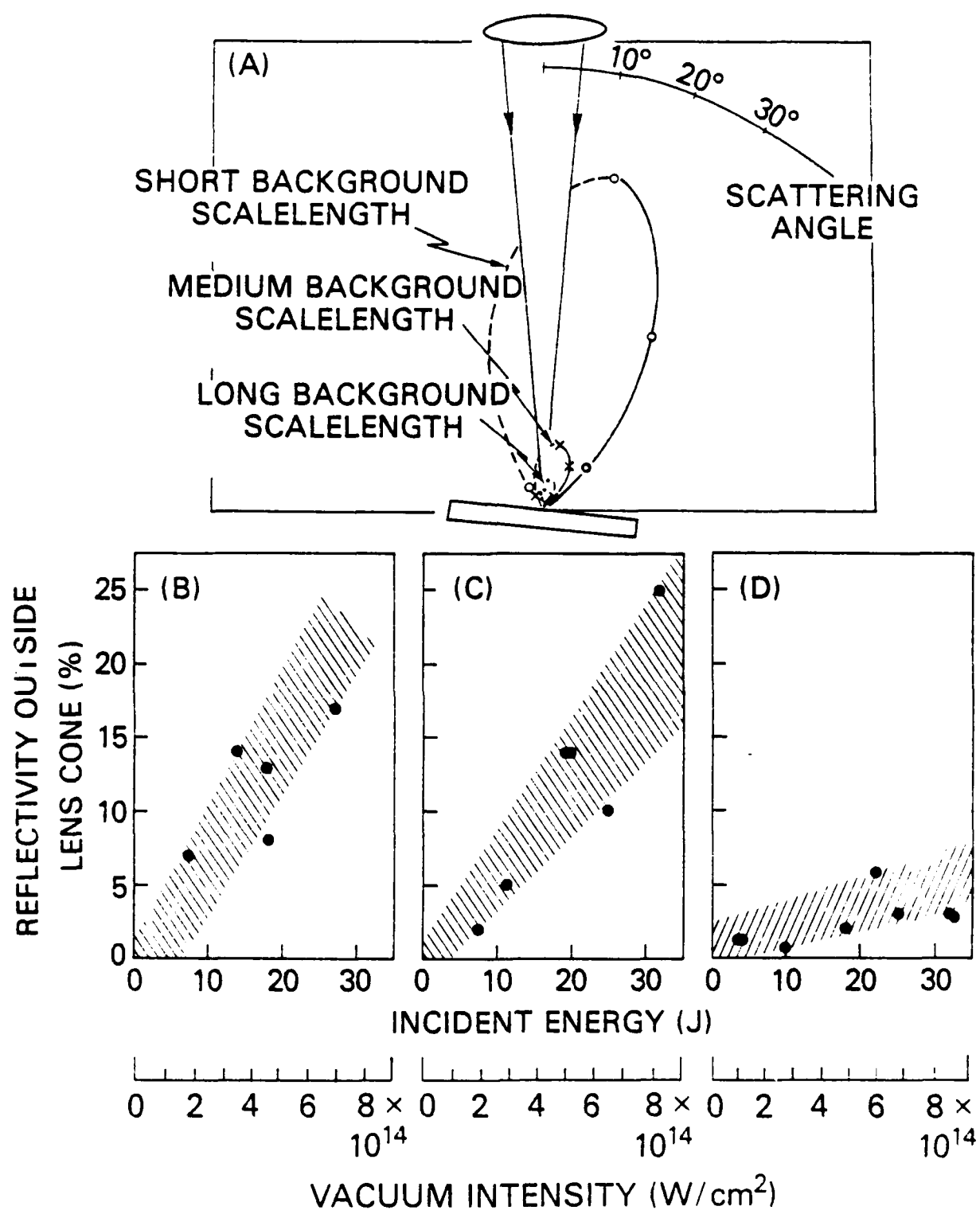


Fig. 5 (A) Angular distributions of light scattered outside the lens cone for  $E = 10$  J. Reflectivities, integrated over angles for: (B) short, (C), medium, and (D) long-scalelength background plasmas.

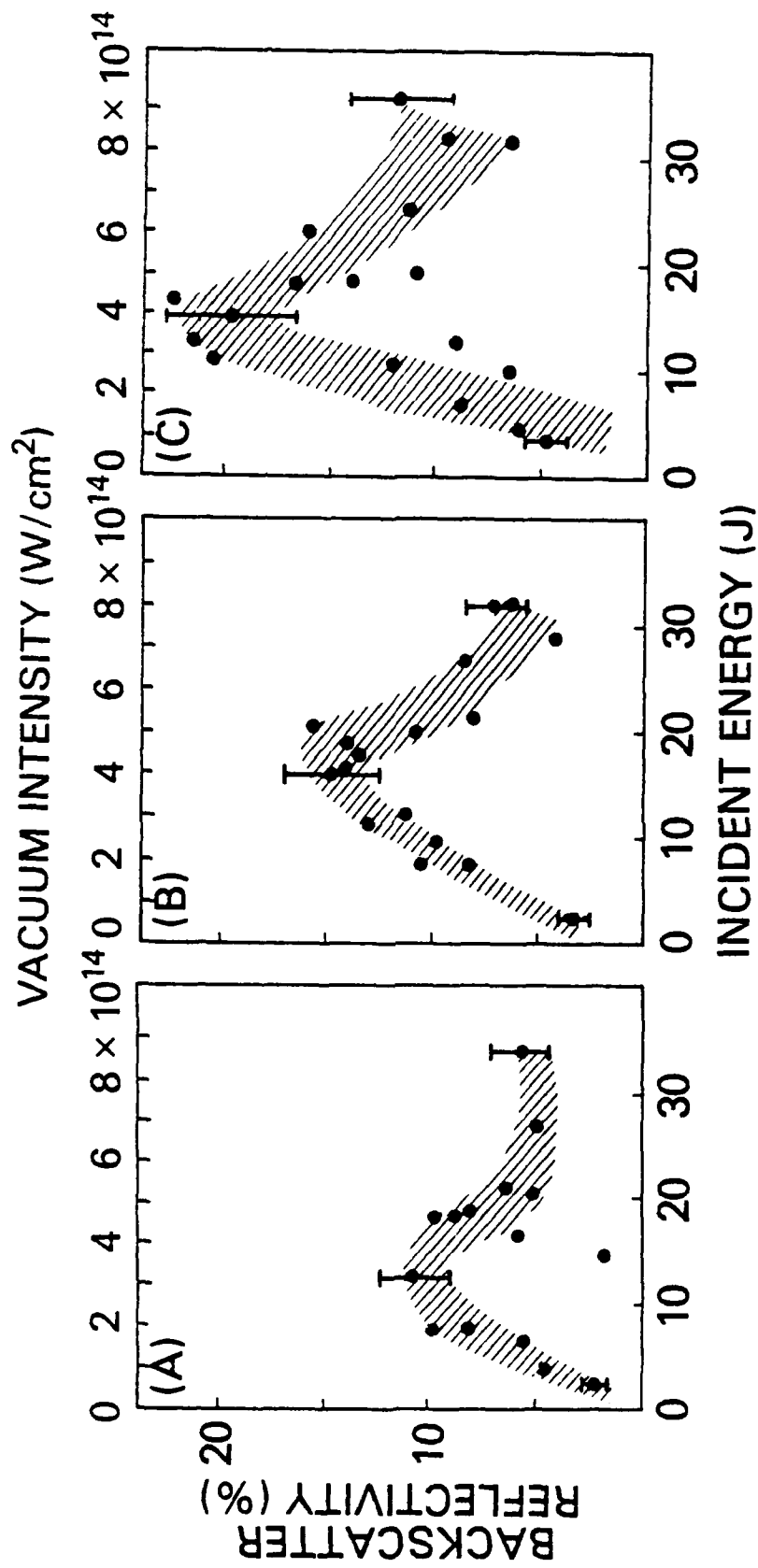


Fig. 6 Backscatter reflectivities for: (A) short, (B) medium, and (C) long-scalelength background plasmas.

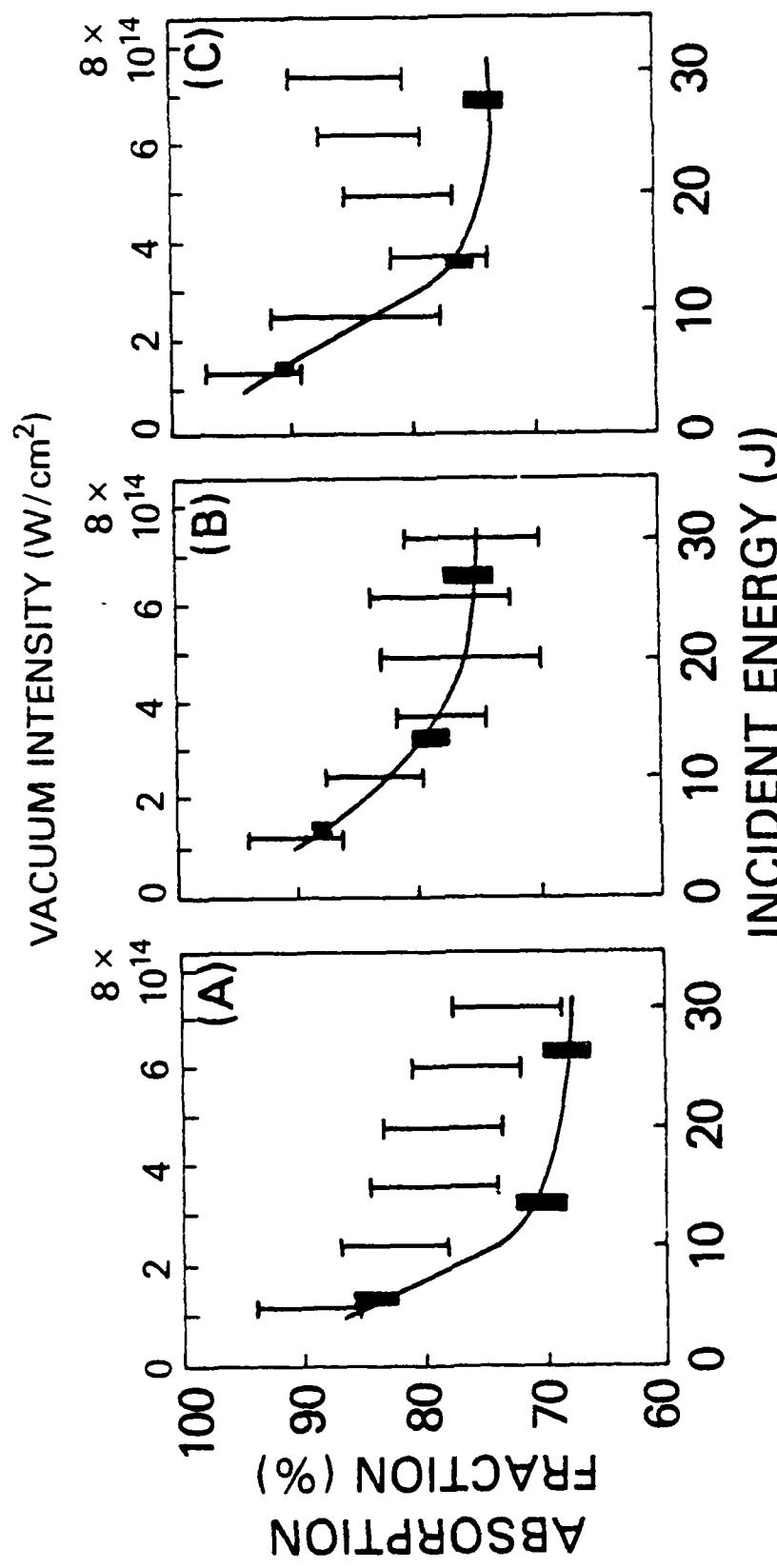


Fig. 7 Comparison between experimental absorption fractions (narrow bars) and calculated collisional absorption (solid curve with wide bars to indicate uncertainties) for (A) short, (B) medium, and (c) long-scalelength background plasma.

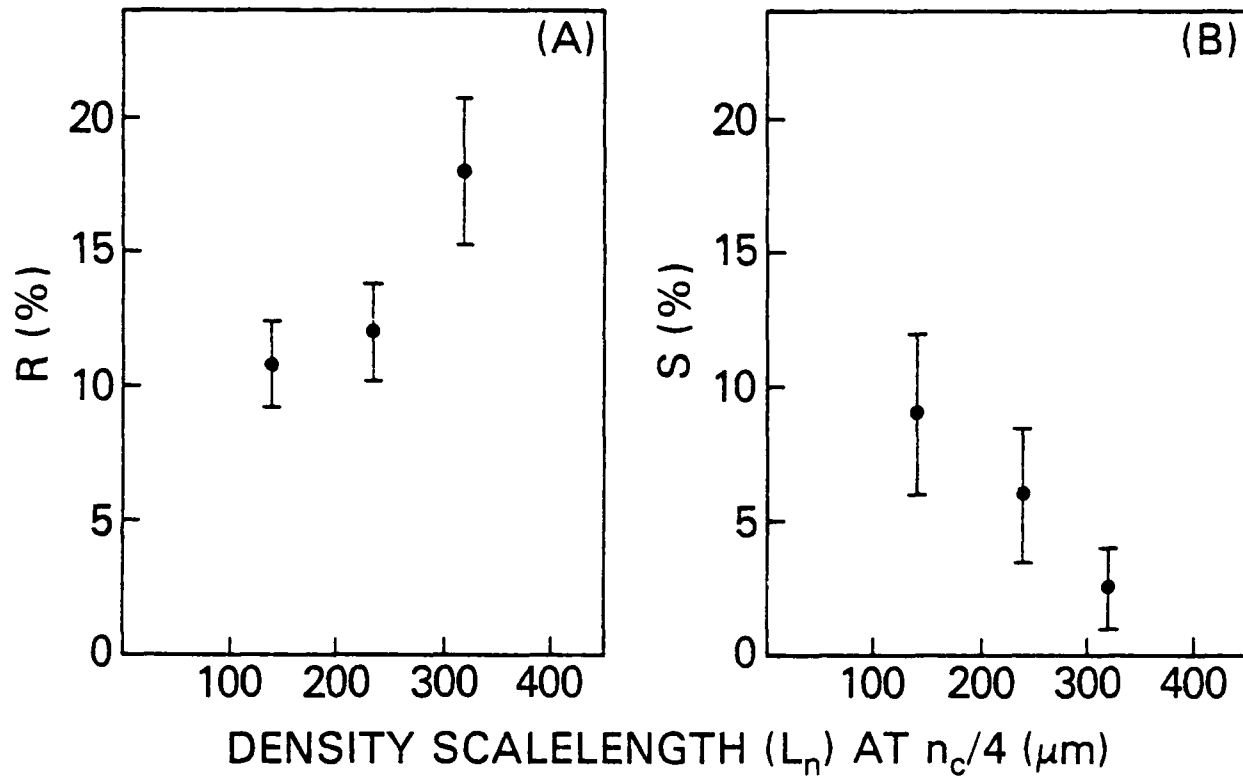


Fig. 8 (A) Backscatter reflectivity through lens, R, and (B) integrated reflectivity over other angles, S, as a function of the density scalelength at quarter-critical density. The scalelength at quarter-critical density is an indicator of underdense scalelength and it is not chosen because absorption is believed to be concentrated near that density.

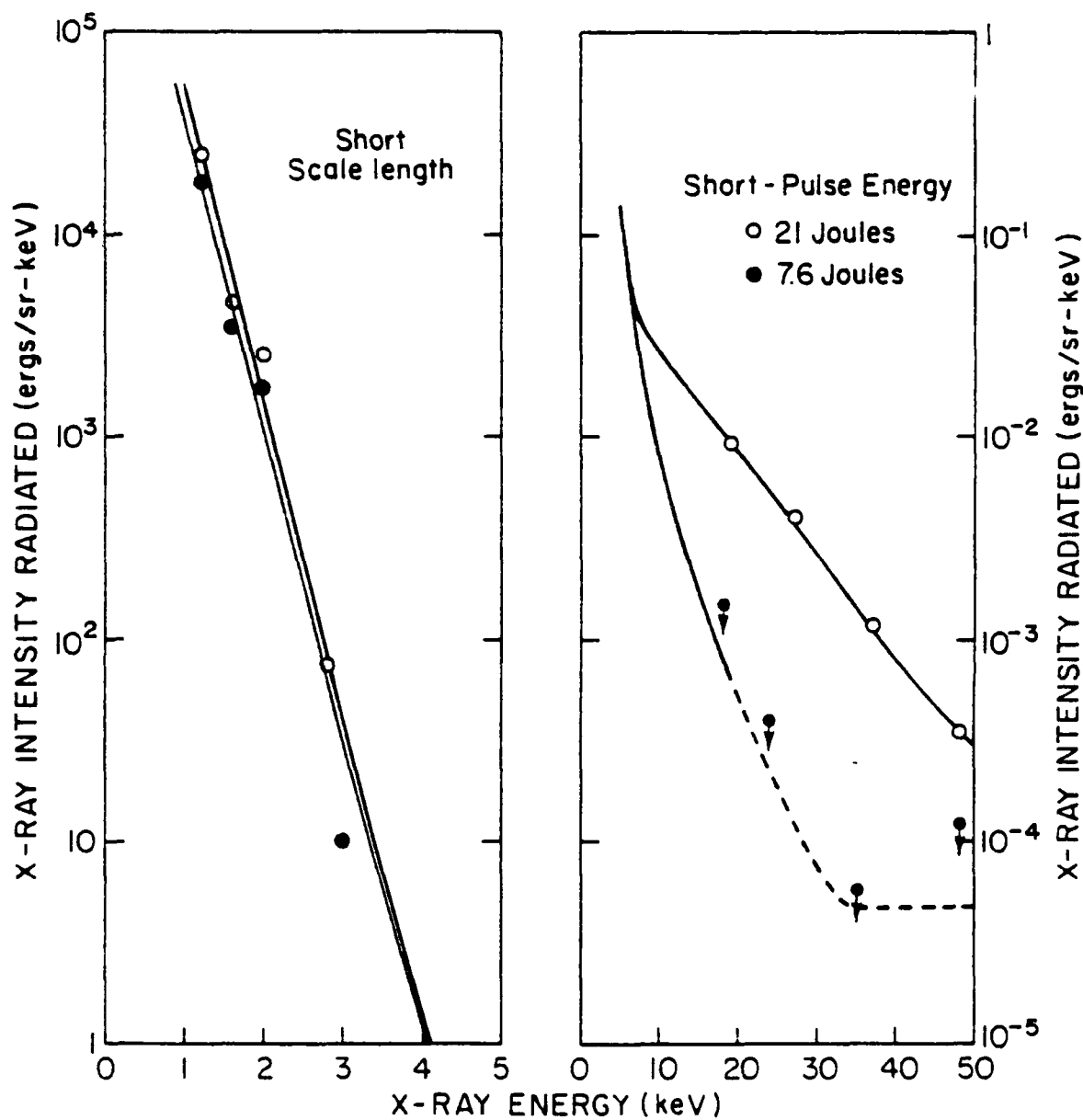


Fig. 9 Typical temporally and spatially-integrated x-ray spectra for the short scalelength condition. The points with arrows are upper limits corresponding to experimental limits of detection.

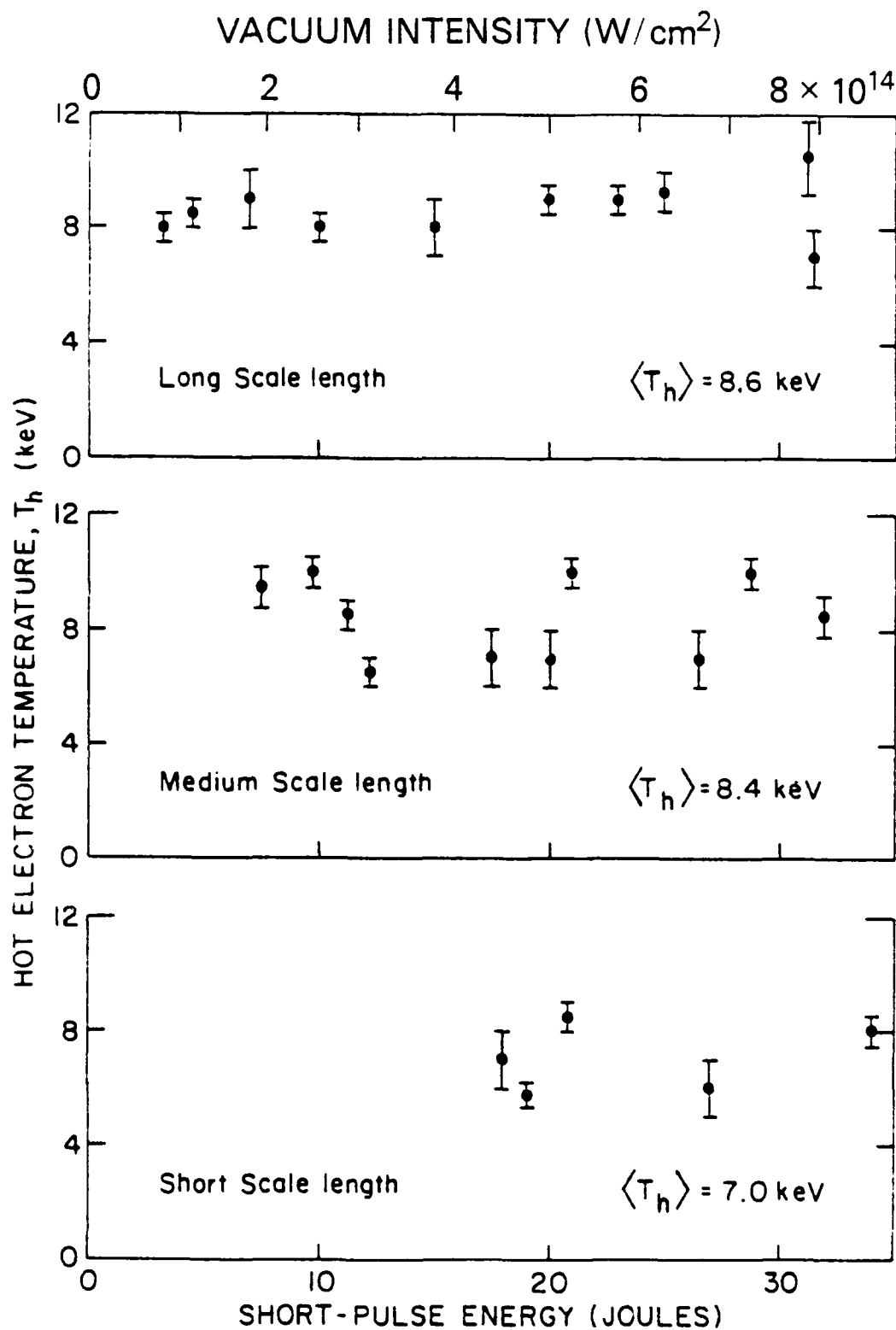


Fig. 10 Hot electron temperatures deduced from high energy (20-50 keV) x-ray spectral measurements for short, medium, and long-scalelength background plasmas.

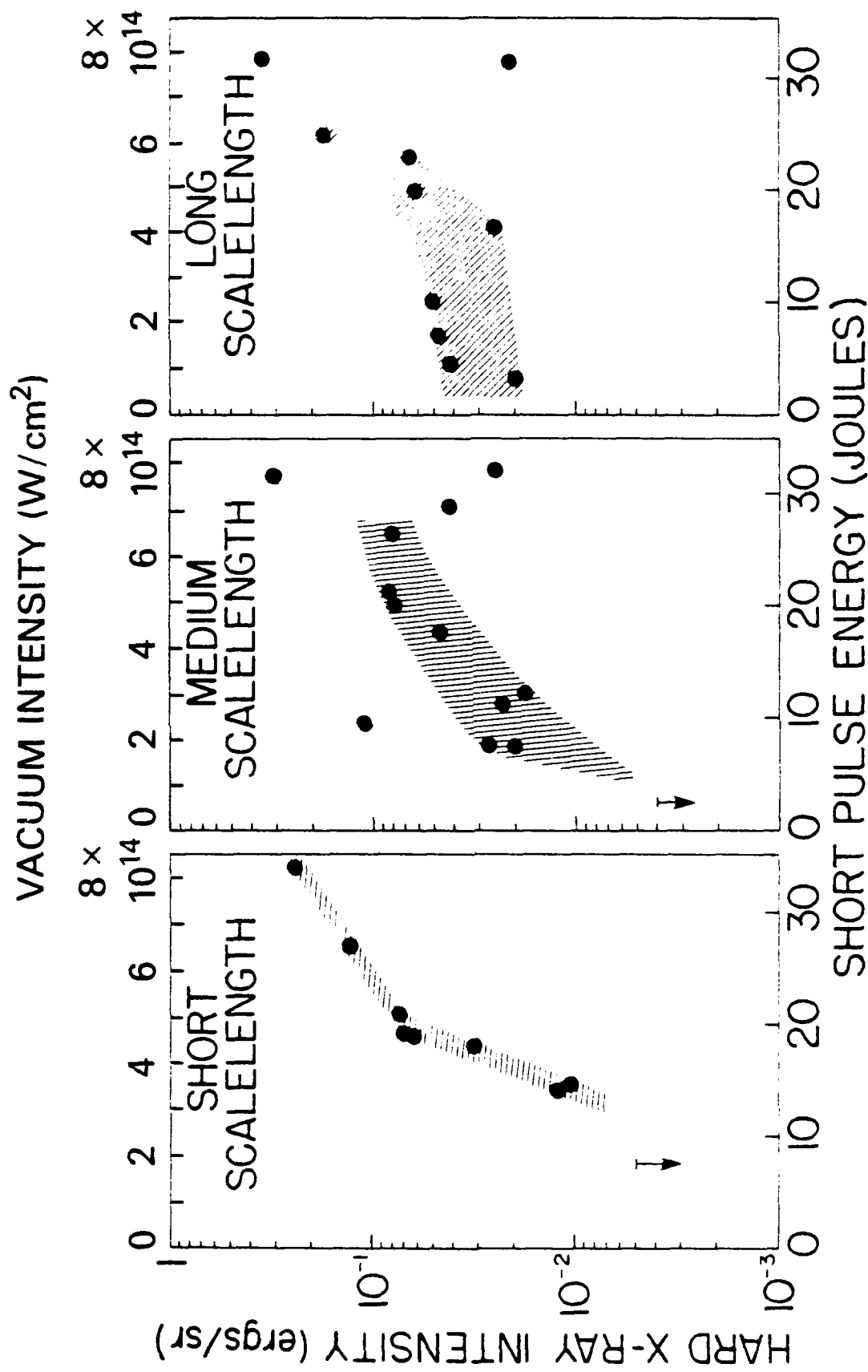


Fig. 11 Energetic x-ray intensities ( $E_{20}$ ) integrated from 20 to 50 keV for different scalelength plasmas. Scatter in the data represents shot-to-shot reproducibility.

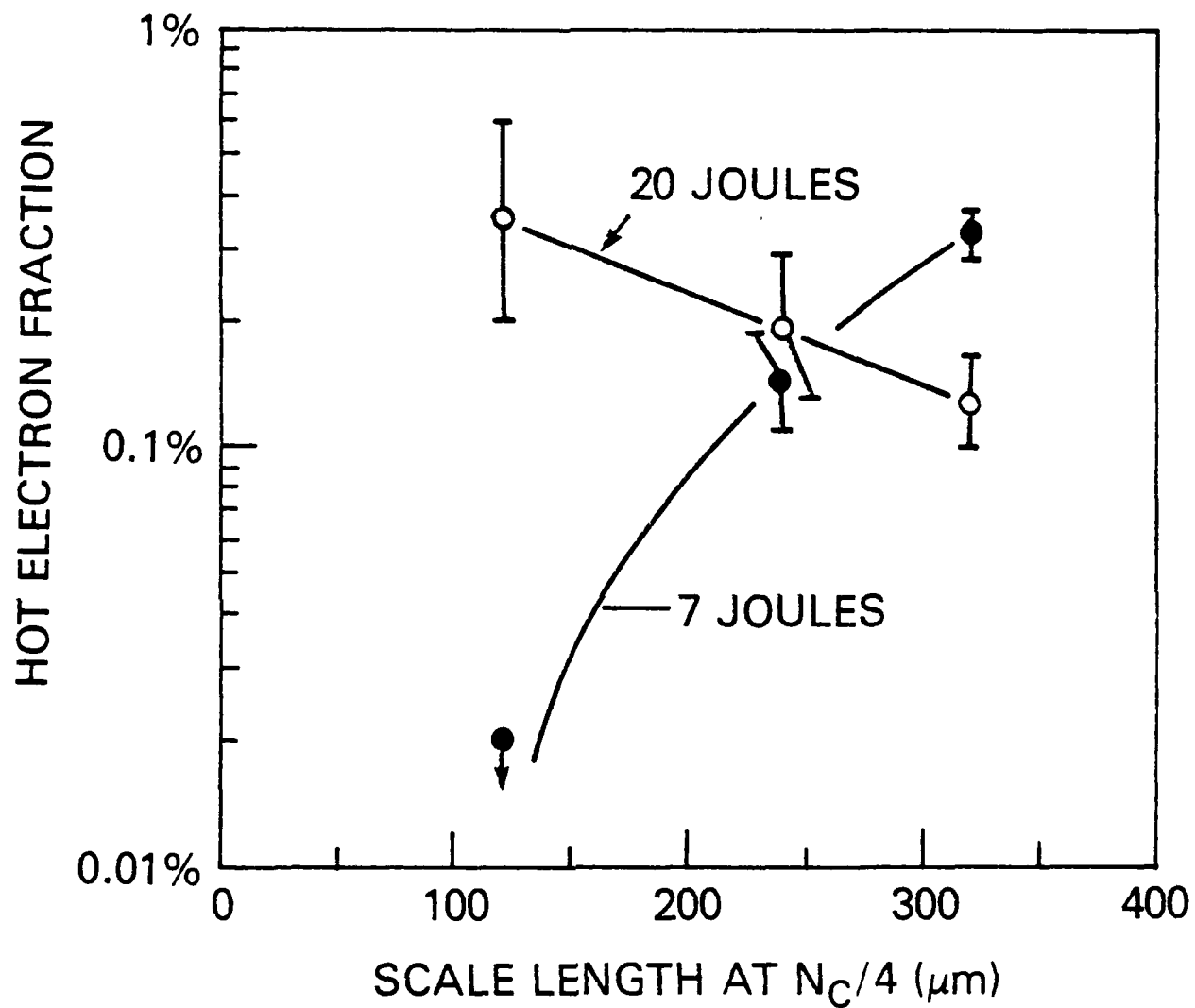


Fig. 12 Hot electron fractions determined from x-ray measurements as a function of the quarter-critical density scalelength. The data point at 7 Joules for the short scalelength is the detection limit.

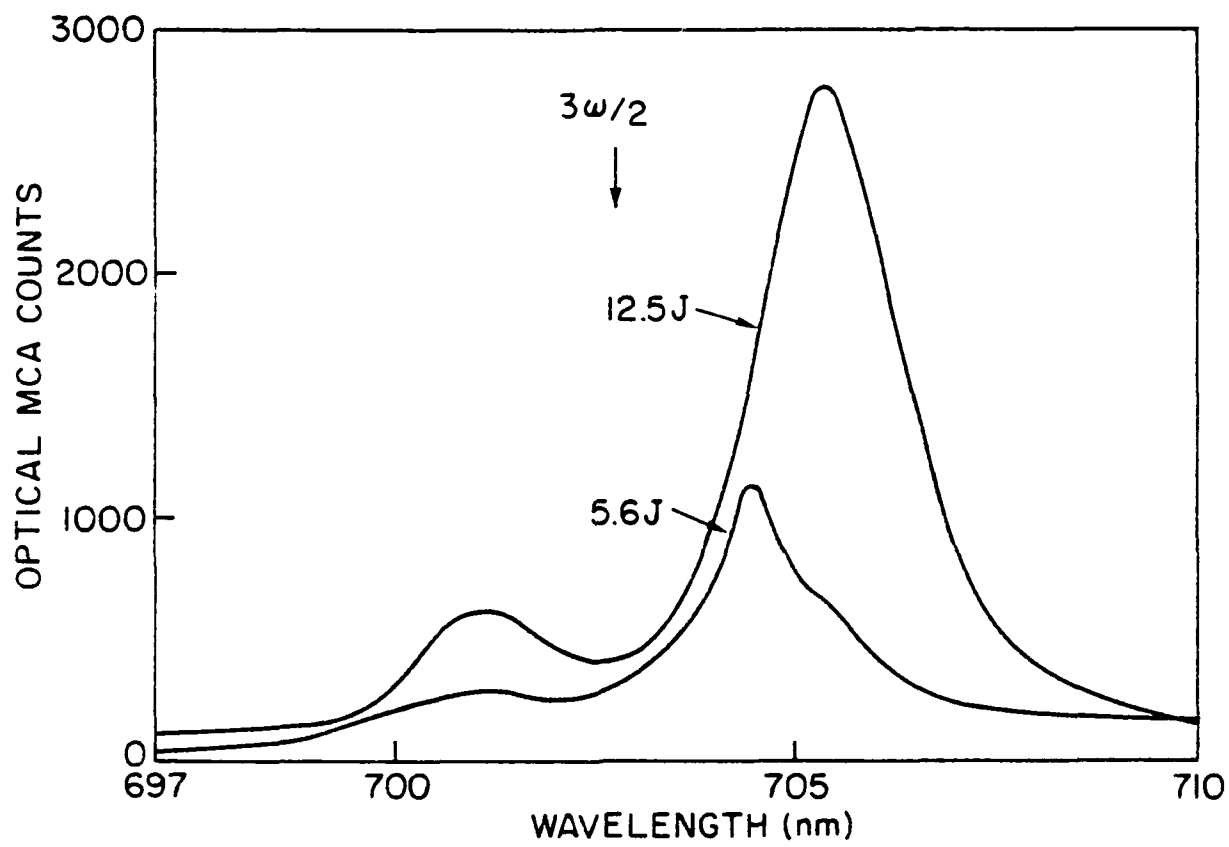


Fig. 13 Spectra of  $3\omega_0/2$  light (uncorrected for CMA response) emitted at  $30^\circ$  to the laser axis. The double-peaked distribution (centered about  $3\omega_0/2$ ) is usually associated with plasma waves driven by the  $\omega_p$  instability.

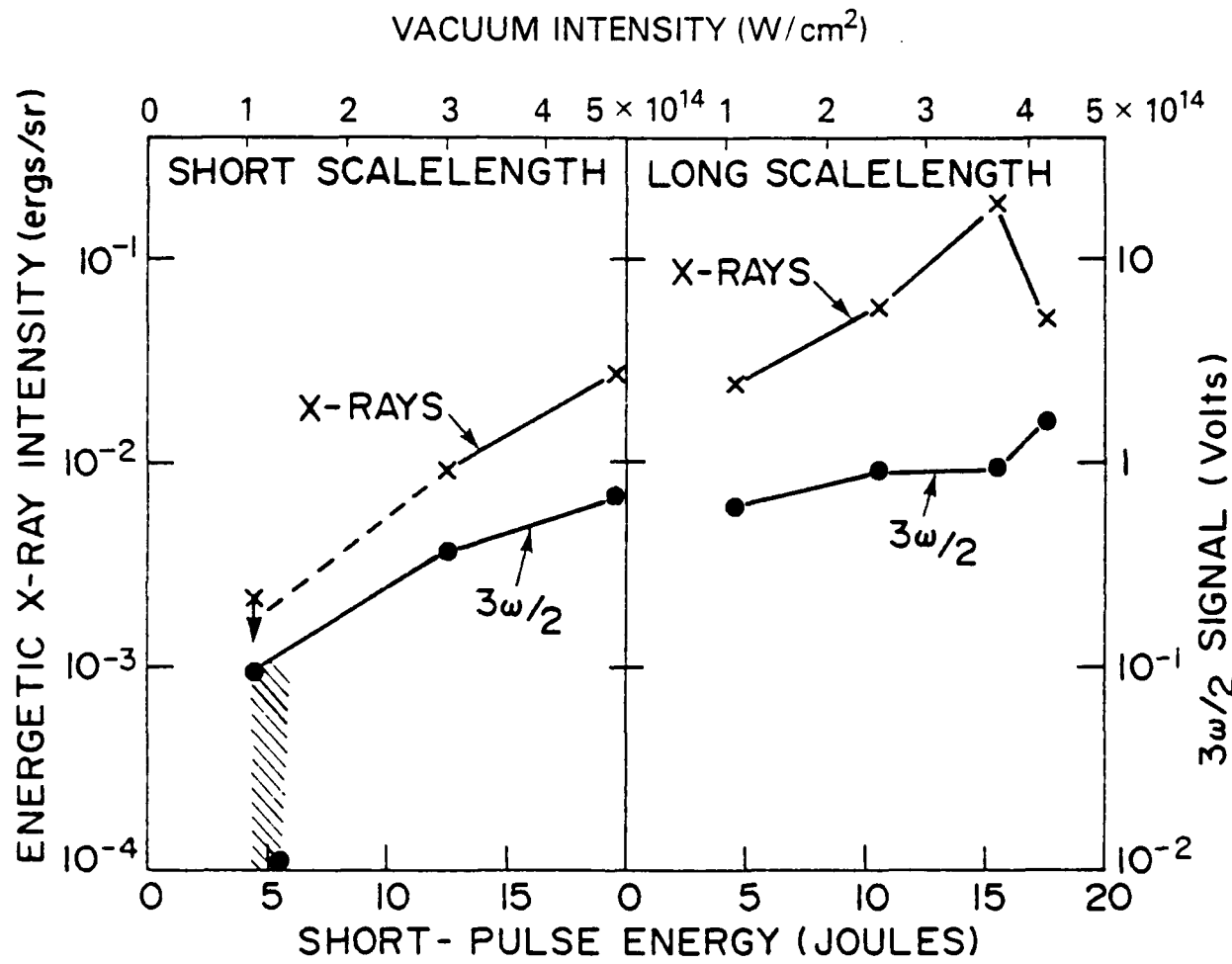


Fig. 14 Energetic x-ray intensity and  $3\omega_0/2$  signal strength for the short and the long-scalelength background plasmas. The data point for energetic x rays at 5 Joules and short scalelength is the detection limit. At the same energy and scalelength the  $3\omega_0/2$  emission increases abruptly by more than order of magnitude.

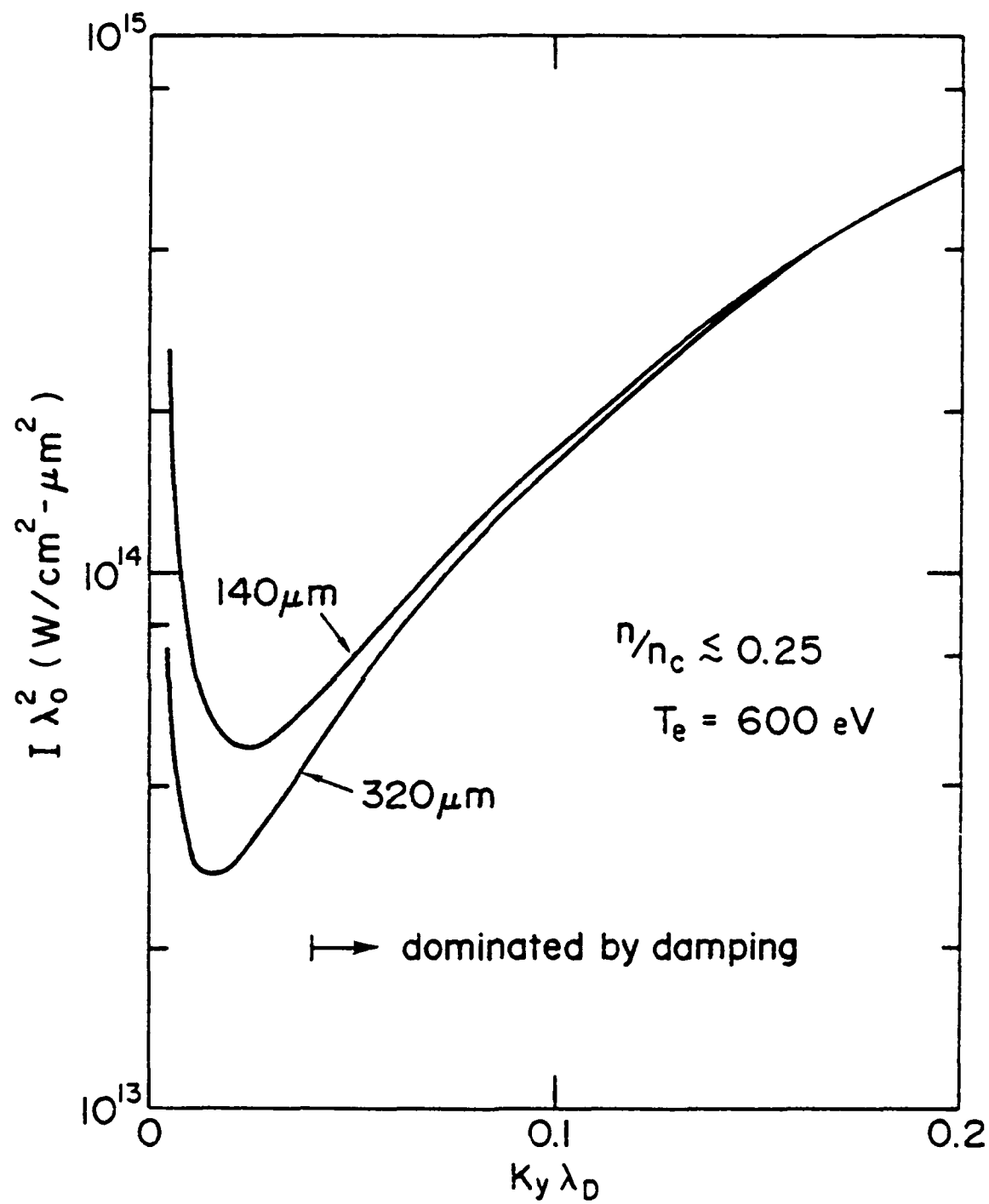
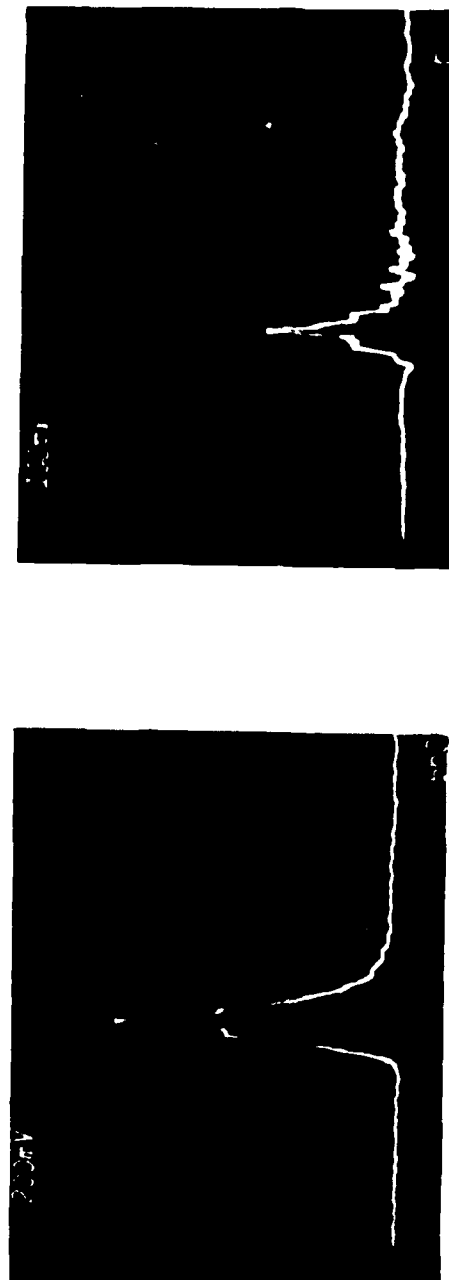


Fig. 15 Threshold values of  $I \lambda_0^2$  for the  $2\omega_p$  instability as a function of transverse wavenumber  $K_y$  in units of the Debye wavelength  $\lambda_D$ .



**Cf Filter (1.5 mil Saran)**

Fig. 16 Oscilloscope traces of two K-edge filter x-ray detectors designed to detect 1-1.5 keV (Al) and 2-2.8 keV (Cf) photons respectively. The ratio of the signal strengths of these two detectors is used to infer plasma temperature.

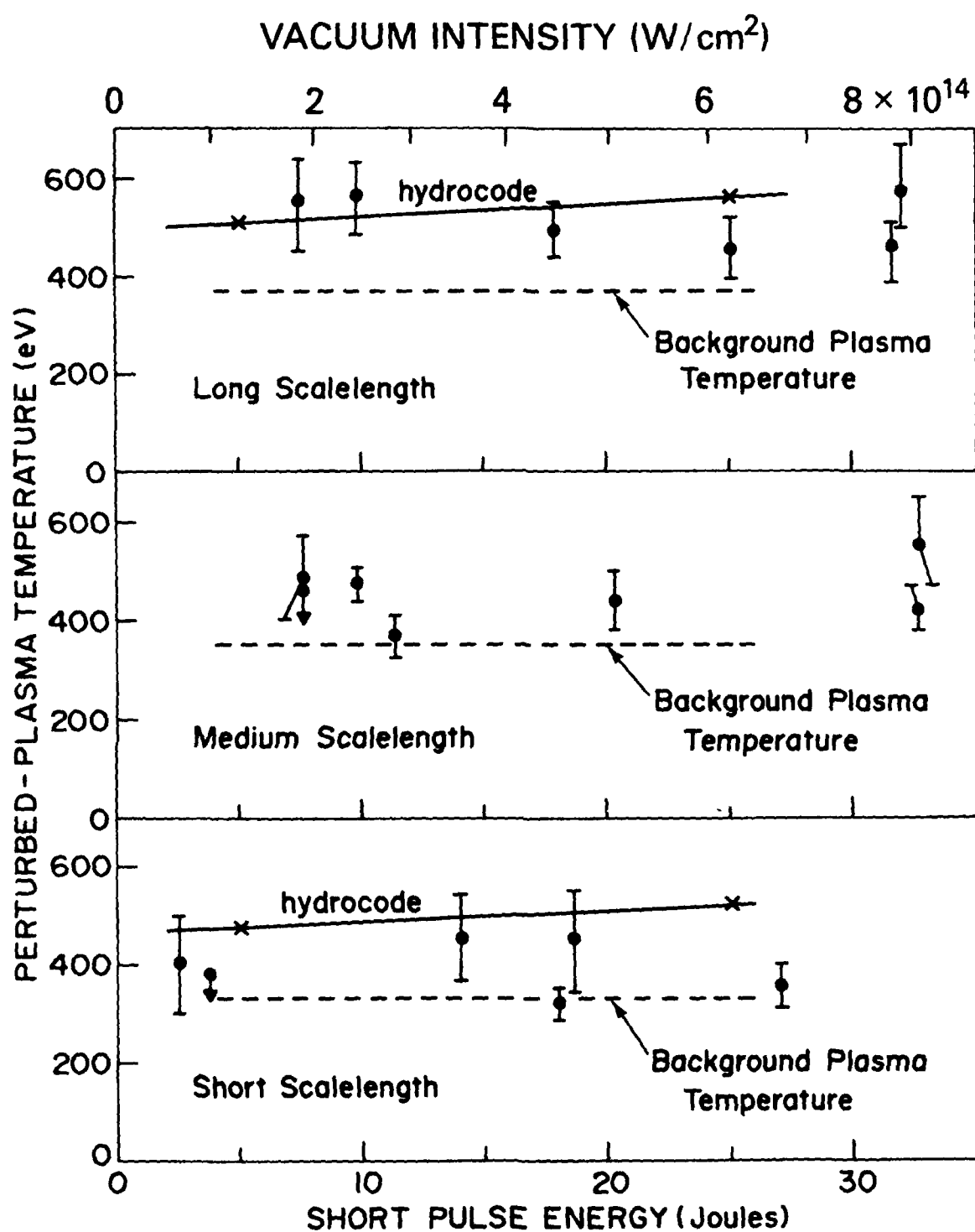


Fig. 17 Perturbed plasma temperatures determined from: 1) the signal strength ratios of the 1-1.5 keV (Al) and 2-2.8 keV (C $\ell$ ) x-ray detectors and 2) the hydrodynamic model for the short, medium, and long-scalelength plasmas.

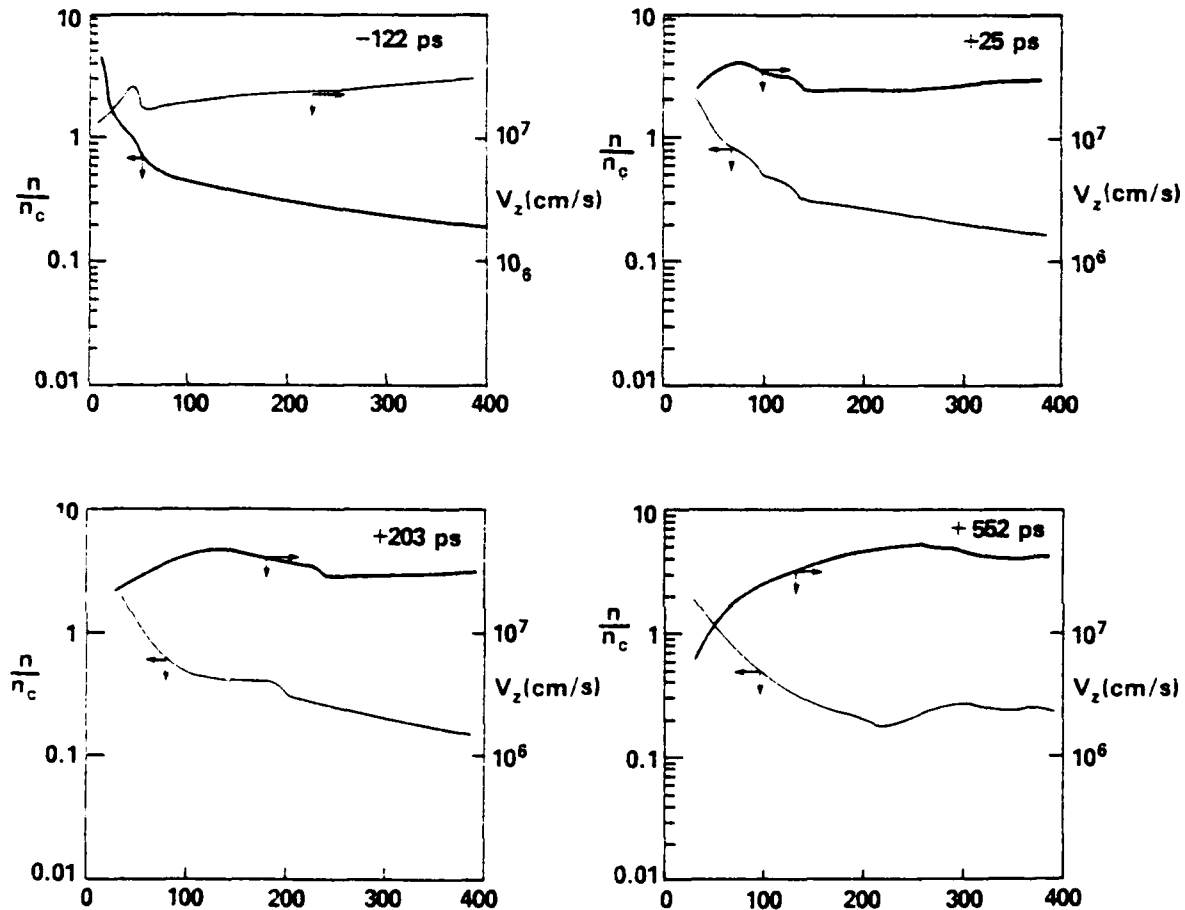


Fig. 18 Axial profiles of density and velocity normal to the target surface for the conditions of the long scalelength plasma with 25 Joules of energy in the short pulse. Plots at successive times from the upper left to the lower right show the progression of an axial shock driven by the short pulse energy. Time is relative to the peak of the short pulse.

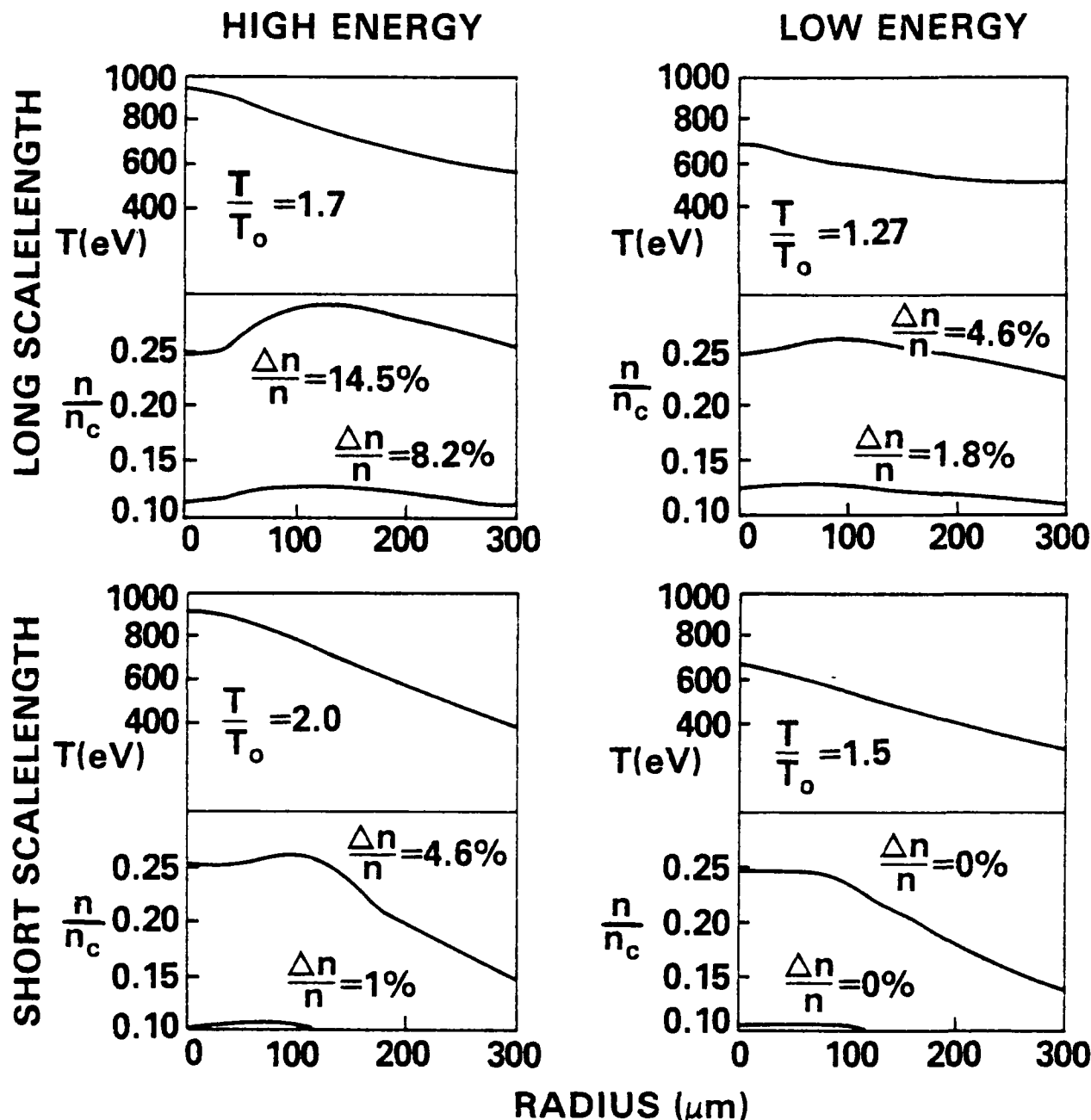


Fig. 19 Computed radial temperature and density profiles at a time near the peak of the short pulse. Results are shown near the quarter-critical and tenth-critical densities for the four conditions of short and long-scalelength and low and high short pulse energy near the extreme values used in the experiment.

## REFERENCES

1. S.E. Bodner, *J. Fusion Energy* 1, 221 (1981).
2. W.L. Kruer, *Comments Plasma Phys. Cont. Fusion* 6, 167 (1981).
3. J.H. Gardner, S.E. Bodner, J.P. Boris, M.H. Emery, M.J. Fritts and M.J. Herbst, in Laser Interaction and Related Plasma Phenomena, eds. H. Hora and G.H. Miley (Plenum, New York, 1984), pp. 673 ff.
4. M.N. Rosenbluth, *Phys. Rev. Lett.* 29, 565 (1972).
5. L.M. Gorbunov, *Zh. Eksp. Teor. Fiz.* 55, 2298 (1968) [Sov. Phys. JETP 28, 1220 (1969)].
6. M.V. Goldman and D.F. DuBois, *Phys. Fluids* 8, 1404 (1965).
7. C.G. Comisar, *Phys. Rev.* 141, 200 (1966).
8. N. Bloembergen and Y.R. Shen, *Phys. Rev.* 141, 298 (1966).
9. E.A. Jackson, *Phys. Rev.* 153, 235 (1967).
10. A.J. Palmer, *Phys. Fluids* 14, 2714 (1971).
11. V.I. Bespalov and V.I. Talanov, *Pis'ma Zh. Eksp. Teor. Fiz.* 3, 471 (1966) [JETP Lett. 3, 307 (1966)].
12. T. Grubl, H. Puehl, and W. Kaiser, *Appl. Phys. Lett.* 25, 135 (1974).
13. R. Massey, K. Berggren, and Z.A. Pietrzyk, *Phys. Rev. Lett.* 36, 963 (1976); R.G. Watt, R.D. Brooks, and Z.A. Pietrzyk, *Phys. Rev. Lett.* 41, 170 (1978).
14. J.T. Turechek and F.F. Chen, *Phys. Rev. Lett.* 36, 720 (1976).
15. A.A. Offenberger, M.R. Cervenan, A.M. Yam and A.W. Pasternak, *J. Appl. Phys.* 47, 1451 (1976); A.A. Offenberger, A. Ny, and M.R. Cervenan, *Can. J. Phys.* 56, 381 (1978).
16. N.H. Burnett, H.A. Baldis, G.D. Enright, M.C. Richardson, and P.B. Corkum, *J. Appl. Phys.* 48, 3727 (1977); H.A. Baldis, J.C. Samson, and P.B. Corkum 41, 1719 (1978).
17. J.J. Schuss, T.K. Chu, and L.C. Johnson, *Phys. Rev. Lett.* 40, 27 (1978).
18. W.T. Armstrong, *J. Appl. Phys.* 49, 2566 (1978).
19. C.R. Neufeld, *J. Appl. Phys.* 51, 237 (1980).
20. F.J. Mayer, G.E. Busch, C.M. Kinzer, and K.G. Estabrook, *Phys. Rev. Lett.* 44, 1498 (1980).

21. P.D. Carter, S.M.L. Sim, and E.R. Woolding, Optics Comm. 32, 443 (1980).
22. C.J. Walsh, J. Meyer, and B. Hilko, Appl. Phys. Lett. 38, 82 (1981); J. Meyer, J.E. Bernard, B. Hilko, H. Houtman, G. McIntosh, and R. Popil, Phys. Fluids 26, 3162 (1983).
23. J. Handke, S.A.H. Rizvi, B. Kronast, Appl. Phys. 25, 109 (1981).
24. D.W. Phillion, E.M. Campbell, K.G. Estabrook, G.E. Phillips, and F. Ze, Phys. Rev. Lett. 49, 1405 (1982).
25. H. Figueira, C. Joshi, H. Azechi, N.A. Ebrahim, and K. Estabrook, Phys. Fluids 27, 1887 (1984).
26. R.P. Drake, R.E. Turner, K.G. Estabrook, B.F. Lasinski, D.W. Phillion, R.L. Kauffman, S.A. Letts, E.A. Williams, E.M. Campbell, C.W. Hatcher, and W.L. Kruer, Proc. 14th Anomalous Absorption Conference (Charlottesville, VA, 1984).
27. C. Labaune, E. Fabre, F. Briand, A. Michard, Proc. 14th Anomalous Absorption Conference (Charlottesville, VA, 1984).
28. H.D. Shay, R.A. Haas, W.L. Kruer, M.J. Boyle, D.W. Phillion, V.C. Rupert, H.N. Kornblum, F. Rainer, V.W. Slivinsky, L.N. Koppel, L. Richards, and K.G. Tirsell, Phys. Fluids 21, 1634 (1978).
29. W. Seka, R.S. Craxton, J. Delettrez, L. Goldman, R. Keck, R.L. McCrory, D. Shvarts, J.M. Soures, and R. Boni, Optics Comm. 40, 437 (1982).
30. C. Garban-Labaune, E. Fabre, C.E. Max, R. Fabbro, F. Amiranoff, J. Virmont, M. Weinfeld, and A. Michard, Phys. Rev. Lett. 48, 1018 (1982).
31. K. Eidmann, G. Brederlow, R. Brodmann, R. Petsch, R. Sigel, G. Tsakiris, R. Volk, and S. Witkowski, J. Phys. D : Appl. Phys. (Great Britain) 12, L145 (1979).
32. M.D. Rosen, D.W. Phillion, V.C. Rupert, W.C. Mead, W.L. Kruer, J.J. Thomson, H.N. Kornblum, V.W. Slivinsky, G.J. Caporaso, M.J. Boyle, and K.G. Tirsell, Phys. Fluids 22, 2020 (1979).
33. H.C. Pant, S. Sharma, and D.D. Bhawalkar, J. Appl. Phys. 51, 6030 (1980).
34. E. McGoldrick and S.M.L. Sim, Optics Comm. 39, 172 (1981).
35. B.H. Ripin, F.C. Young, J.A. Stamper, C.M. Armstrong, R. Decoste, E.A. McLean, and S.E. Bodner, Phys. Rev. Lett. 39, 611 (1977).
36. E.T. Fabrikesi and T.A. Hall, J. Phys. D : Appl. Phys. (Great Britain), 13, L131 (1980).
37. R. Decoste, P. Lavigne, H. Pepin, G.R. Mitchel, and J.C. Kieffer, J. Appl. Phys. 53, 3505 (1982).

38. D.W. Phillion, D.L. Banner, E.M. Campbell, R.E. Turner, and K.G. Estabrook, *Phys. Fluids* 25, 1434 (1982).

39. E.M. Campbell, M.D. Rosen, D.W. Phillion, R.H. Price, K. Estabrook, B.F. Lasinski, S.P. Obenschain, E.A. McLean, R.R. Whitlock, and B.H. Ripin, *Appl. Phys. Lett.* 43, 54 (1983).

40. R.P. Drake, R.E. Turner, B.F. Lasinski, K.G. Estabrook, E.M. Campbell, C.L. Wang, D.W. Phillion, E.A. Williams, and W.L. Kruer, Lawrence Livermore National Laboratory Report UCRL-91371 (1984), to be published.

41. D.W. Phillion, W.L. Kruer and V.C. Rupert, *Phys. Rev. Lett.* 39, 1529 (1977).

42. E.M. Campbell, in Radiation in Plasmas, ed. B. McNamara (World Scientific Pub. Co., Singapore, 1984), V. 1, pp. 579 ff.

43. B. Arad and S. Eliezer, *Appl. Phys. Lett.* 32, 401 (1978).

44. M.J. Herbst, J. Grun, J. Gardner, J.A. Stamper, F.C. Young, S.P. Obenschain, E.A. McLean, and B.H. Ripin, *Phys. Rev. Lett.* 52, 192 (1984).

45. F.C. Young, M.J. Herbst, C.K. Menka, S.P. Obenschain, and J.H. Gardner, *Phys. Rev. Lett.* 54 2509 (1985).

46. J.A. Stamper, R.H. Lehmberg, A. Schmitt, M.J. Herbst, F.C. Young, J.H. Gardner, and S.P. Obenschain, NRL Memorandum Report No. 5462 (1984, to be published).

47. M.J. Herbst, P.G. Burkhalter, D. Duston, M. Emery, J. Gardner, J. Grun, S.P. Obenschain, B.H. Ripin, R.R. Whitlock, J.P. Apruzese, and J. Davis, in Laser Interaction and Related Plasma Phenomena, V. 6, eds. H. Hora and G.H. Miley (Plenum New York, 1984), pp. 317 ff.

48. M.J. Herbst, P.G. Burkhalter, J. Grun, R.R. Whitlock, and M. Fink, *Rev. Sci. Instrum.* 53, 1418 (1982).

49. P.G. Burkhalter, M.J. Herbst, D. Duston, J. Gardner, M. Emery, R.R. Whitlock, J. Grun, J.P. Apruzese, and J. Davis, *Phys. Fluids* 26, 3650 (1983).

50. D. Duston and J. Davis, NRL Memorandum Report No. 5038. (AD-125 755)

51. F.C. Young, in Naval Research Laboratory Memorandum Report No. 3591, 1977, edited by S.E. Bodner, pp. 41ff. (AD-A050 089)

52. R.D. Evans, The Atomic Nucleus (McGraw-Hill, New York, 1955) pp. 614ff.

53. M.J. Herbst, F.C. Young, J.A. Stamper, K.J. Kearney, J. Grun, J.H. Gardner, S.P. Obenschain, E.A. McLean and B.H. Ripin, in Radiation in Plasmas, edited by B. McNamara (World Scientific Publishing Co., Singapore, 1984) Vol. 1, pp. 407 ff.

54. C.S. Liu, M.N. Rosenbluth and R.B. White, *Phys. Fluids* 17, 1211 (1974).

55. C.S. Liu, in Advances in Plasma Physics, edited by A. Simon and W.B. Thompson (Wiley, New York, 1976) Vol. 6, p. 121.

56. D.W. Forslund, J.M. Kindel and E.L. Lindman, Phys. Fluids 18, 1002 (1975).

57. J.F. Drake and Y.C. Lee, Phys. Rev. Lett. 31, 1197 (1973).

58. M.N. Rosenbluth, R.B. White and C.S. Liu, Phys. Rev. Lett. 31, 1190 (1973).

59. C.S. Liu and M.N. Rosenbluth, Phys. Fluids, 19, 967 (1976).

60. B.F. Lasinski and A.B. Langdon in Lawrence Livermore Laboratory Laser Program Annual Report, edited by C.F. Bender and B.D. Jarmam, UCRL-50021-77, 19078, Vo.. 2, pp. 4-49 (unpublished).

61. A. Simon et al. Phys. Fluids 26, 3107 (1983).

62. F.F. Chen, Introduction to Plasma Physics, (Plenum, New York, 1974) pp. 213 ff.

63. M.A. Heald and C.B. Wharton, Plasma Diagnostics with Microwaves (John Wiley and Sons, New York, 1965) pp. 57ff.

64. W.L. Kruer, Phys. Fluids 15, 2423 (1972).

65. A.B. Langdon, B.F. Lasinski, and W.L. Kruer, Phys. Rev. Lett. 43, 133 (1979); K. Estabrook and W.L. Kruer, Phys. Fluids 26, 1892 (1983).

66. H.A. Baldis and C.J. Walsh, Phys. Fluids 26, 1364 (1983).

67. J.G. Pronko and L.F. Chase, Nucl. Instr. and Meth. 164, 79 (1979).

68. J. McMahon, R. Lahmberg, B. Ripin and J. Stamper, in Naval Research Laboratory Memorandum Report No. 3315, 1976, edited by S.E. Bodner, pp. 20ff (AD-A029 408)

69. W.L. Kruer, Phys. Fluids 23, 1273 (1980).

70. C.S. Liu, M.N. Rosenbluth, and R.B. White, Phys. Fluids 17, 1211 (1974).

71. This expression is similar to Eq. (36) of Ref. 53.

72. R.H. Lehmburg, V.K. Tripathi, and C.S. Liu, Phys. Fluids 24, 703 (1981).

73. I.M. Begg and R.A. Cairns, J. Phys. D : Appl. Phys. (Great Britain) 9, 2341 (1976).

74. C.J. Randall, J.R. Albritton, and J.J. Thomson, Phys. Fluids 24, 1474 (1981).

END

FILMED

3 - 86

DTIC